Geochimica et Cosmochimica Acta 421 (2026) 82–96

Contents lists available at ScienceDirect

Geochimica et Cosmochimica Acta

journal homepage: www.elsevier.com/locate/gca

Insights into silicon isotopic fractionation during reverse weathering from *in vitro* incubations of sediments from a temperate estuary

Zhe Dong [a,*], Katharine Hendry [a,b], James M. Byrne [a], Casey Bryce [a], Tong Wang [a], Hong Chin Ng [a], Jamie Lewis [a]

[a] School of Earth Sciences, University of Bristol, Bristol, UK
[b] British Antarctic Survey, Cambridge CB3 0ET, UK

ARTICLE INFO

Associate Editor: Lixin Jin

Keywords:
Reverse weathering
Authigenic phases formation
Stable Si isotopes
Severn Estuary
Sediment incubation

ABSTRACT

Authigenic precipitation of clay minerals in marine sediments, termed reverse weathering, is an important process in global biogeochemical cycles due to its role in regulating alkalinity and nutrient budgets. Dissolved silicon (silicic acid) is inherently linked with reverse weathering and is a key nutrient required by a major algal group, diatoms. Previous research has suggested that diatom biogenic silica (BSi) provides an important component for reverse weathering reactions. Stable silicon isotope measurements of extracted reactive sediment 'pools' reveal that there is a strong isotopic fractionation associated with this authigenic precipitation, and are a potentially useful tool for tracing these reactions. However, previous reverse weathering studies have largely focused on tropical and subtropical deltaic environments, with less attention paid to temperate estuaries. Here, we use a two-year sediment incubation experiment with samples collected from the Severn Estuary (UK) to investigate reverse weathering processes in temperate estuary sediments. We present the first experimental constraint on silicon isotopic fractionation during the initial stage of the precipitation of amorphous authigenic phases, with fractionation factors ($^{30}\varepsilon_{RW\_authi\text{-}solution}$) ranging from −2.20 ‰ ± 0.45 ‰ (1σ) to −4.61 ‰ ± 0.47 ‰ (1σ), which is larger than previous estimates. This high degree of fractionation may help explain the strongly fractionated silicon isotope compositions observed in both reactive solid phase pools and pore fluids where reverse weathering is active. Our comparison of sterilized and non-sterilized samples demonstrates that reverse weathering type reactions can occur abiotically. However, microbial activity and the sediment mineralogy can still affect the reverse weathering type reactions, by competing for key elements in the porewaters, modulating redox cycles or promoting the rapid neoformation of authigenic phases. The use of glass beads as a substrate demonstrates that the dissolution of amorphous silica, analogous to diatom BSi, can obscure the silicon isotope fractionation signal in the porewater. These findings highlight the significant influence that biological activity and sediment composition can have on reverse weathering, offering new insights into its dynamics in different sedimentary environments.

1. Introduction

Reverse weathering, originally postulated as the reconstitution of degraded aluminosilicates (Mackenzie and Garrels, 1966) and subsequently demonstrated to include the precipitation of cation-rich authigenic phases on siliceous templates (Michalopoulos and Aller, 1995), plays a critical role in regulating the oceanic cycling of a wide range of elements (Ehlert et al., 2016; Huang et al., 2024; Isson and Planavsky, 2018; Ku and Walter, 2001; Li et al., 2021; Loucaides et al., 2010; Mackenzie and Kump, 1995; März et al., 2015; Michalopoulos and Aller, 1995, 2004; Pickering et al., 2020; Rahman et al., 2016, 2017; Rahman et al., 2019; Santiago Ramos et al., 2018; Trapp-Müller et al., 2025; Zhang et al., 2022; Zhao et al., 2025). While the term has been applied to a range of sedimentary processes, here we use reverse weathering to refer specifically to the incipient authigenic precipitation of amorphous to poorly crystalline phases from porewaters (Michalopoulos and Aller, 2004; Zhao et al., 2025). These reverse weathering reactions involve the uptake of dissolved cations and silicon (silicic acid, or DSi) from porewaters into solid mineral forms (Ehlert et al., 2016; Loucaides et al., 2010; Pickering et al., 2020). Early *in vitro* experiments from sediments

* Corresponding author.
E-mail address: dongzhe2997@163.com (Z. Dong).

https://doi.org/10.1016/j.gca.2026.04.015
Received 7 July 2025; Accepted 9 April 2026
Available online 12 April 2026

from the Amazon basin revealed that diatom biogenic silica (BSi) provides a key source of dissolved silicon for reverse weathering reactions, and the BSi frustules can serve as substrates for authigenic formations (Loucaides et al., 2010; Michalopoulos and Aller, 1995, 2004; Michalopoulos et al., 2000). In coastal settings, this process is estimated to sequester up to 50% of riverine dissolved silicon flux, representing a major sink for silicon in the ocean (Michalopoulos and Aller, 2004; Rahman et al., 2017).

Stable silicon (Si) isotope measurements are a potentially useful tool for tracing these reverse weathering reactions, as strong isotopic fractionation is known to occur during authigenic mineral precipitation and has been found in *in vitro* mineral precipitation experiments (e.g., Geilert et al., 2014; Wang et al., 2021). Modelling studies, based on observations of sedimentary pore fluid profiles from a range of environmental settings, support a substantial silicon isotope fractionation during authigenic clay mineral formation (Ehlert et al., 2016; Ng et al., 2020; Wang et al., 2024; Ward et al., 2022). For example, recent in situ measurements of marine authigenic clays have directly constrained their silicon isotopic composition, revealing light δ^{30}Si values ranging from −2.24 ‰ to −3.17 ‰ and confirming strong fractionation during reverse weathering (Geilert et al., 2024). Furthermore, sequential leaching techniques, which use specific chemical reagents to isolate distinct sedimentary silica phases, have revealed extremely light silicon isotope signatures in the acid-leachable fractions (associated with poorly crystalline aluminosilicates and metal oxides). This distinctive isotopic depletion serves as a key tracer for reverse weathering, as the precipitation of authigenic minerals preferentially incorporates light silicon isotopes from the porewater (Pickering et al., 2020; Wang et al., 2024; Ward et al., 2022). However, there is a lack of direct experimental evidence for reverse weathering and its impact on isotopic fractionation in natural sediments, resulting in several outstanding questions. Firstly, while it is established that biological productivity supplies the essential siliceous reactant (BSi), the influence of benthic microbial activity on the reverse weathering mechanism itself remains poorly constrained. Specifically, it is not yet clear how microbial metabolism, through the alteration of porewater pH and redox conditions, may facilitate or inhibit the precipitation of authigenic phases. Secondly, the influence of sediment composition on the extent and nature of reverse weathering reactions is also not well understood. Thirdly, it remains unclear how the silicon budget and isotopic fractionation associated with reverse weathering are influenced by the combined effects of biological activity and sediment composition. These knowledge gaps limit the application of silicon isotopes as tracers of marine biogeochemical processes, both in contemporary oceans and throughout Earth's history.

Coastal and estuarine environments are favourable settings for reverse weathering to occur, as they receive abundant terrestrial inputs of essential reactants, including reactive aluminosilicates, metal oxides, and dissolved ions, which are required for authigenic phases precipitation (Loucaides et al., 2010; Michalopoulos et al., 2000). The Severn Estuary, the largest tidal estuary in Europe, serves as a major transition zone for this land–ocean material transport (Kirby, 2010; Langston et al., 2010; Wallington et al., 2023). Therefore, sediments collected from this terrestrially influenced system provide an ideal substrate to constrain the geochemical potential for reverse weathering in temperate estuaries. In this study, we conducted a two-year sediment incubation experiment to investigate the occurrence of reverse weathering type reactions and to quantify its impact on silicon isotope fractionation. By comparing treatments with and without microbial activity, and with different substrate additions representing varied sediment compositions, we examine how biological activity and sediment mineralogy influence the reverse weathering process. Our results provide new experimental evidence for silicon isotope fractionation during reverse weathering type reactions and demonstrate that this process can exert a major influence on silicon cycling even under dynamic estuarine conditions.

2. Methodology

2.1. Study area and sampling

The Severn Estuary, located between South Wales and South-West England (Fig. 1), is the largest hyper-tidal estuary in Europe and features the second highest tide range in the world, with a mean spring range of 12.3 m and a mean neap range of 6.5 m (Kirby, 2010; Langston et al., 2010). It serves as a vital coastal transition zone between the River Severn, the longest river in the UK, and the Bristol Channel, ultimately discharging into the Irish Sea and the North Atlantic. The estuary's unique hydrodynamics, influenced by its funnel-shaped profile and strong tidal resonance, create extreme sediment resuspension and intense vertical mixing (Wallington et al., 2023). These factors, combined with the high tidal energy, make the Severn Estuary one of the most dynamic estuarine systems in the world. The intense tidal energy in this system facilitates the continuous supply and reworking of terrestrial materials, creating a geochemical environment with high potential for reverse weathering reactions.

Sample collection was undertaken at upper Severn Estuary (Fig. 1) during daylight hours at low tide on 12th October 2021. Fresh intertidal mudflat sediment was collected using 50 mL centrifuge tubes and stored in the freezer at −20 °C. One river water sample was collected at River Wye, which flows directly past the sediment sampling site before entering the Severn Estuary (Fig. 1), and was therefore considered representative of the riverine input interacting with the sampled sediments. The water sample was immediately filtered in the field using pre-cleaned 20 mL syringes and 0.22 μm filters (Sartorius Minisart® Syringe Filter, Polyethersulfone). Subsamples of river water were acidified with double-distilled HCl (0.1% v/v) for elemental and isotopic analyses.

2.2. Sediment incubation experiment

2.2.1. Incubation setup

The incubation experiment built on the approach of Michalopoulos and Aller (1995), who simulated Amazon delta conditions by adding substrates to fresh Amazon sediments to observe reverse weathering type reactions using scanning electron microscopy (SEM) and transmission electron microscopy (TEM). In our study, we replicated this setup under temperate estuarine conditions by using in situ sediments and river water, and expanded on their findings by incorporating isotopic measurements alongside SEM and energy dispersive X-ray spectroscopy (EDS) analyses. We have adapted the substrates used from their experiment, to be more relevant for conditions in the Severn Estuary. These substrates investigated include:

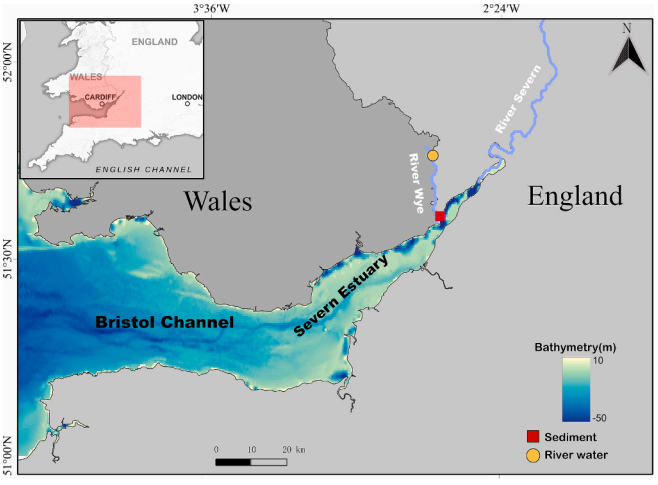

Fig. 1. Bathymetry map of the Severn Estuary and sample locations (Gebco Bathymetric Compilation Group, 2022).

(1) Kaolinite (Sigma-Aldrich, CAS: 1318-74-7), representing the typical cation-poor aluminosilicate minerals in the Severn Estuary.
(2) Quartz sand (100–500 μm, VWR International Ltd), another typical transported estuarine sediment component.
(3) Iron (Fe) (oxyhydr)oxide (FeOOH)-coated quartz (Hereafter referred as iron-coated quartz), representing the common metal oxides in the sediments.
(4) Glass beads (1.5–16 mm, SiLibeads® Type M soda-lime glass), simulating the biogenic silica generated from diatoms (Michalopoulos and Aller, 1995). Chemically, these beads are dominated by SiO_2, Na_2O, and CaO. Physically, the beads are characterized by a highly polished surface and high sphericity (Roundness $\geq$ 0.98).

Additional substrates include:

(5) Iron (Fe) (oxyhydr)oxide-coated glass beads (Hereafter referred as iron-coated glass beads), representing the mineral-coated diatom.
(6) Blank (pure sediments without additional substrate, to compare with the experiments with substrate additions).

Frozen sediments were thawed at room temperature the day before the incubation setup. Thawed sediments were mixed by gentle stirring, after which 80 g of sediments were subsampled and stored in the freezer as initial samples. Quartz sand and glass beads were coated with 2-line ferrihydrite, which was synthesized following the procedure outlined in Sorwat et al. (2020). It should be noted that the iron-oxide coating procedure may result in a non-homogeneous distribution of Fe on the quartz and glass bead surfaces. To quantify the iron content in the coated sand and glass beads, the Ferrozine assay (Stookey, 1970) was applied on the coated quartz sand and glass beads, the results indicated 1.31 mg_{Fe}/g_{quartz} and 0.46 mg_{Fe}/g_{glass}.

One gram of each substrate (0.5 g for kaolinite) was weighed, placed onto pre-autoclaved Teflon sheets, and secured with sterile cable ties. It is important to note that the quantities of each substrate used in this study do not reflect natural environmental concentrations. Substrate masses (1 g for most substrates; 0.5 g for kaolinite, reduced due to its low bulk density) were selected following the experimental approach of Michalopoulos and Aller (1995), with the aim of providing sufficient material for post-incubation characterization while remaining compatible with the physical constraints of the incubation tubes. For context, the clay mineral fraction of Severn Estuary sediments is dominated by illite (~58%), expandable minerals (~28%), kaolinite (~12%) and chlorite (~5%), with quartz representing approximately 25% of the total suspended sediment (Allen, 1991; Manning et al., 2010). The added kaolinite and quartz substrates therefore represent relatively modest additions to the naturally abundant clay minerals and quartz already present in the sediment matrix. In contrast, biogenic silica constitutes only a minor component of total sediment mass in this high-turbidity estuary, and the glass bead loading likely overestimates the natural proportion of amorphous silica. These differences between experimental and natural substrate proportions should be considered when extrapolating the results to natural open systems.

Evenly distributed holes were pierced in these Teflon bags to enable the free flow of porewater between the substrates and sediments. The whole Teflon bag making procedure was performed under a laminar fume hood to prevent contamination. Incubations were conducted under anoxic conditions to simulate the reducing environment characteristic of early diagenesis in these deltaic sediments. This oxygen-free setting ensures the stability of dissolved Fe^{2+}, preventing its removal as Fe-oxides and maintaining its availability as a critical reactant for the precipitation of Fe-rich authigenic silicates (Michalopoulos and Aller, 1995; Michalopoulos et al., 2000; Zhang et al., 2022). To remove oxygen and ensure an anoxic environment for the reverse weathering experiment, sediments (500 g) and river water (320 mL) were flushed with nitrogen gas for 30 min to remove ambient oxygen. Half of the homogenized sediments and river water were autoclaved (121 °C and 15 psi) to sterilize any present microbes, to investigate the role of microbes in the reverse weathering type reactions. Substrates used in both sterile and non-sterile sets were separately sterilized using UV (30 min) instead of autoclaving, as high temperatures could induce the transformation from synthesized ferrihydrite to a more crystalline phase such as hematite. Additionally, all the plastic utensils used in this experiment, including pipette tips, beakers and spatulas, were autoclaved to avoid biological contamination.

The whole incubation set-up procedure was performed in an anoxic glovebox (95% N_2: 5% H_2) to guarantee an anoxic environment for the incubation. Pre-prepared substrates in Teflon bags were first inserted into the pre-labelled sample tubes. Homogenized and sterilized sediments were weighed and equally divided (approximately 12.5 g per portion), which were then transferred into 10 mL sterile sample tubes. They were divided into 6 sets (triplicates for each set), corresponding to the first 6 experimental treatments described above. Two additional sets of substrate-free incubation tubes, one sterile and one non-sterile, were included to assess the potential impact of differing sample extraction strategies applied at the year one and year two intervals (see Section 2.2.2).

The same volume (8 mL) of natural river water was added into each tube, acting as the overlying water. Subsequently, tubes were capped within the anaerobic glovebox, sealed with parafilm and placed into Kilner Jars, which were also filled with N_2 (100%). After the initial setup and sealing within the glovebox, the tubes were removed from the glovebox and incubated at room temperature (~20 °C) in the dark for 12–24 months. The airtight integrity of the tubes was monitored using oxygen indicator strips (Anaerotest™ Strips, Merck), ensuring that anoxic conditions were maintained throughout the duration of the experiment. The sediment incubation setup is shown in the schematic figure (Fig. 2).

2.2.2. Sample retrieval

After one year of incubation, overlying water, porewater and sediment samples were retrieved from all replicates of each sample. Sample extraction was carried out under a laminar flow hood, with N_2 gas flow constantly flushing above the sample tubes, to minimise oxidation. 2 mL of overlying water sample was pipetted from each sample tube and transferred into acid-cleaned Eppendorf tubes. 1 mL of the sediment-porewater mixture from the upper few centimetres (Fig. 2) was retrieved and transferred into acid-cleaned Eppendorf tubes. The sample tubes were immediately capped after completing the extraction and placed back into the Kilner Jar. It should be noted that the removal of approximately 2 mL of overlying water (~25% of the initial aqueous volume) and a smaller proportion of the solid phase during Year 1 sampling effectively reduced the water/rock (W/R) ratio for the second year of incubation. The potential influence of this modified W/R ratio on authigenic precipitation is discussed in Section 4.1.2.1 and Section 4.3. After the completion of sample extraction, the sample tubes were placed into the anoxic glovebox overnight with their caps slightly loosened, to remove any possible infiltrated oxygen during the extraction. The next morning, caps were tightened before the tubes were removed from the glovebox. The sample tubes were then sealed with parafilm and stored at room temperature (~20 °C, approximating mean ambient temperatures of the Severn Estuary in June to August, ranging from 18 to 21 °C) (Severn Estuary Partnership) in the dark for another year of incubation. Eppendorf tubes with sediments were centrifuged at 13,400 rpm for 10 min (Eppendorf minispin®). Upon completion, the supernatant porewaters were carefully removed and transferred into acid-cleaned Eppendorf tubes. The remaining sediment samples were then stored in the freezer for the future analyses. Centrifugation and sample transfer operations were performed outside the glovebox. To minimize oxidative artifacts, the overlying and porewater samples were acidified

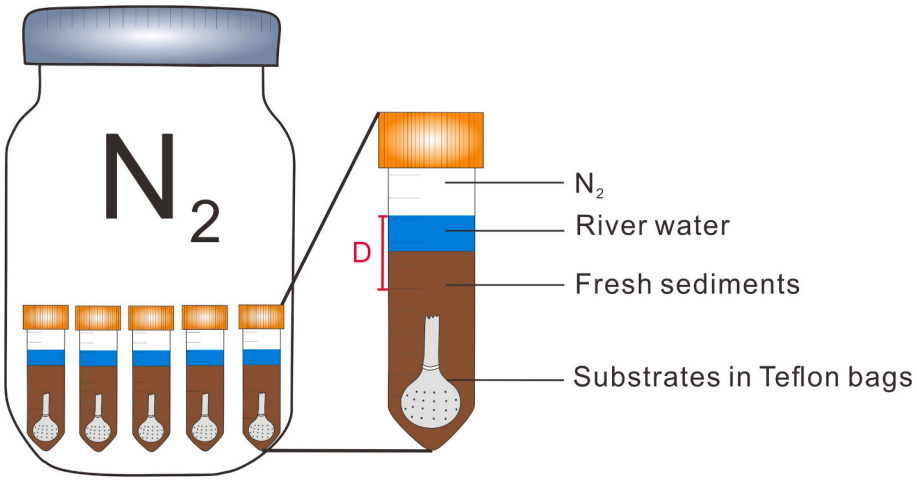

Fig. 2. Schematic illustrating the setup of the sediment incubation experiment. The red vertical bar 'D' represents the approximate depth of sample extraction at one-year interval.

immediately with double distilled HCl (0.1% v/v) after centrifugation. This acidification step effectively arrests biological uptake and prevents the precipitation of Fe and Mn (hydr)oxides, ensuring the preservation of dissolved species for analysis and avoiding the potential fractionation of Si isotopes by biological uptake or adsorption on Fe and Mn (hydr) oxides (Lin et al., 2011; Massmann et al., 2004; Ward et al., 2022).

The incubation was terminated after two years. After termination, the overlying water samples were first extracted by carefully pipetting under the laminar flow hood, with N_2 gas flow constantly flushing above the sample tubes. The inserted substrate bags were subsequently withdrawn. To prevent the potential transformation of the newly formed minerals through oxidation, substrates were fished out using a clean steal hook inside the anaerobic glovebox and left inside the glovebox for a week to be air-dried. The sediments were centrifuged at 4000 rpm for 20 min for the porewater extraction. The supernatant porewaters were carefully pipetted out and transferred into the acid-cleaned Eppendorf tubes. The remainder sediments were stored in the freezer for the future analyses. The retrieved overlying water and porewater samples were acidified with double distilled HCl (0.1% v/v), for elemental and isotopic measurements.

2.3. Solid samples extraction and digestion

Three operationally defined silicon pools were sequentially extracted from sediment samples following protocols adapted from Pickering et al. (2020) and Ward et al. (2022): (1) highly reactive silica associated with metal oxides and poorly crystalline authigenic precipitation (Si–HCl), (2) biogenic silica and their amorphous diagenetically altered products (Si–Alk), and (3) soluble lithogenic silica and refractory biogenic silica (Si–NaOH).

Frozen sediments were thawed at room temperature, and ~0.12–0.15 g (wet weight) were transferred to 50 mL polyethylene centrifuge tubes. Sediments were never dried or ground during extraction, as such treatments can significantly alter Si contents and isotopic compositions (Ward et al., 2022). Subsamples were oven-dried at 60 °C only to determine dry-to-wet weight ratios. Organic matter was removed by treatment with 5 mL of 10% H_2O_2 followed by 30 min sonication (Mortlock and Froelich, 1989). Samples were then rinsed three times with ultra-pure water, with centrifugation (4000 rpm, 10 min) between rinses.

Highly reactive silica (Si–HCl) was extracted by leaching sediments with 36 mL of 1 N HCl (in-house distilled) at room temperature for 18 h. Leachates were centrifuged, filtered (0.22 μm, Sartorius Minisart® Syringe Filter, Polyethersulfone), neutralized using 4 M NaOH, and stored for Si concentration and isotope analyses. Residual sediments were rinsed three times to remove residual acid. Rinse solutions were discarded as they contain negligible Si (Rahman et al., 2016).

BSi and their amorphous diagenetically altered products (Si–Alk) was extracted by leaching the HCl-treated sediments with 40 mL of 0.1 M Na_2CO_3 at 85°C for 5 h. A 10 mL aliquot was withdrawn after 20 min, immediately acidified with 1 N HCl to terminate dissolution, filtered (0.22 μm), and retained for Si isotope analysis, as early leachates predominantly reflect BSi with minimal lithogenic interference (Demaster, 1981; Michalopoulos and Aller, 2004; Pickering et al., 2020). Additional aliquots were collected at 2, 3, and 5 h, acidified, and analysed for Si concentrations. Dissolution kinetics were used to distinguish biogenic from lithogenic silica, with BSi contents estimated by extrapolating the linear dissolution trend back to time zero (Demaster, 1981; Michalopoulos and Aller, 2004).

Finally, soluble lithogenic silica and refractory biogenic silica (Si–NaOH) was extracted by leaching the remaining sediments with 10 mL of 4 M NaOH at 85 °C for 2 h. Leachates were filtered (0.22 μm), combined with filtered rinse solutions, neutralized 10 N HCl, and stored for subsequent Si concentration and isotope analyses. It is important to note that these operationally defined Si pools have their limitations and could oversimplify the complexity of Si distribution in the sediments. Chemical extractions rely on solubility differences rather than strict mineralogical boundaries, inevitably aggregating heterogeneous phases into a single pool (Zhang et al., 2023).

Carbonate-oxide fraction and silicate fraction were sequentially extracted from wet sediments (10–20 mg) to track the intensity of sediment dissolution using the radiogenic Sr isotopes ($^{87}Sr/^{86}Sr$). Samples were dried, treated with 30% H_2O_2 (ROMIL SpA) to remove organics, and re-dried. Carbonate-oxide were leached using 3 N HNO_3 (1.9 mL, 120°C overnight). The mixture was centrifuged (13,400 rpm, 10 min), and the supernatant was collected. The remaining sediment, as well as the Teflon beaker that was used for the carbonate-oxide leaching, were rinsed with 1 mL ultra-pure water three times. The nitric acid and three rounds of ultra-pure water rinses were combined and dried down. This combination is regarded as the carbonate-oxide fraction in the sediment samples, which was eventually dissolved in 5 mL of 2% (v/v) nitric acid for the $^{87}Sr/^{86}Sr$ measurements. The well rinsed sediment was then digested with the concentrated HF-HCl-HNO_3 mixture, with a HF: HCl: HNO_3 ratio of 1:1:4. After the complete digestion, the solution was dried down and refluxed in 6 N HCl twice, and eventually dissolved in 10 mL of 2% (v/v) nitric acid for the element analysis, as the silicate fraction in the sediment.

Five substrates used in the incubation experiment were digested using a mixture of HF and HNO_3 (HF: HNO_3 = 1:4) at 150 °C in cleaned Teflon vessels. The solutions were refluxed twice in 6 N HCl at 120 °C

and eventually dissolved in 3 N HNO_3.

2.4. Acronyms for samples

The following acronyms are used in this study to differentiate:

(1) Sterilization: sterile or non-sterile.
(2) Substrates: blank, kaolinite, quartz, iron-coated quartz, glass beads and iron coated glass beads.
(3) Sample types: porewater, overlying water and sediment.

A summary and description of each acronym is illustrated in Table 1.

2.5. Geochemical analyses

The geochemical analyses of elemental concentrations and isotopic compositions were conducted at the Bristol Isotope Group laboratories at the University of Bristol. Data reproducibility of samples is assessed in Supplementary information (Supplementary Text S1, Fig. S1 and Fig. S2).

2.5.1. Elemental concentrations

The concentrations of all elements, including Na, Mg, Ca, K, Sr, Fe, Mn, Al, Li, Cu and Si in the solution samples were analysed using the ICP-MS Element2 (Thermo Fisher Scientific). Samples were spiked with 5 ppb indium for internal normalization and subsequently calibrated to concentrations using a multi-element standard. The long-term reproducibility of all elements, except for Si, was evaluated using the BIR-1 reference basalt. For Si, a river water sample with a known DSi concentration was used to assess reproducibility. The long-term relative standard deviation (RSD, 1σ) across all elements ranged from 7.61% to 17.2%, with an average of 11.1%. The reporting limit of concentration for all elements in this study is 20 ppb.

2.5.2. Isotopic compositions

2.5.2.1. Si isotopes. Si isotopes were separated via column chromatography (Georg et al., 2006b) using Bio-Rad AG50W X12 resin. High-salinity samples (e.g., porewater and incubated overlying water) underwent pre-concentration using the Magnesium Induced Co-precipitation (MAGIC) method (de Souza et al., 2012; Karl and Tien, 1992). Post-column samples were doped with Mg (10 ppm, Inorganic Venture Mg Standard), 0.1 M H_2SO_4 and 1 N HCl to correct for instrumental mass bias and matrix effects (Cardinal et al., 2003; Hughes et al., 2011). Si isotopes were measured on a Neptune MC-ICP-MS (Thermo Finnigan) using standard-sample bracketing technique (De la Rocha, 2002). The $\delta^{29}Si$ and $\delta^{30}Si$ values for all samples and standards analysed in this study align with a mass-dependent fractionation line, exhibiting a slope of 0.5119 ($R^2 = 0.998$). The long-term reproducibility of the Si isotope measurement was verified using three reference materials: LMG08 (sponge spicules), diatomite and ALOHA (seawater) at 1000 m, yielding the mean $\delta^{30}Si$ value of −3.41 ‰ ± 0.15 ‰ (2σ, n = 37), +1.25 ‰ ± 0.13 ‰ (2σ, n = 29), and +1.25 ‰ ± 0.17 ‰ (2σ, n = 12), respectively, in keeping with the previously reported values (Grasse et al., 2017; Hendry et al., 2011; Reynolds et al., 2007).

2.5.2.2. Radiogenic Sr isotopes. In addition to stable Si isotopes, radiogenic Sr isotopic ratios ($^{87}Sr/^{86}Sr$) were determined in order to trace the influence of sediment and substrate dissolution on porewater geochemistry during incubation. The measurement procedure of $^{87}Sr/^{86}Sr$ ratio is described in the Supplementary Information (Text S2, Fig. S3).

Table 1
Acronyms used in this study to differentiate substrate types.

Explanation of acronyms component	Example
First letter indicates the sterilization condition: **S**: Sterilized **N**: Non-Sterilized The middle letter(s) signifies the different substrates: **B**: Blank **K**: Kaolinite **Q**: Quartz **IQ**: Iron-coated quartz **GB**: Glass beads **IGB**: Iron-coated glass beads Letter(s) at the end represents the sample type: **PW**: Porewater **OW**: Overlying water **S**: Sediment	Example 1. **S-B-PW**: Sterilized blank porewater sample Example 2. **N-GB-S**: Non-Sterilized glass beads sediment sample

2.6. SEM and EDS

SEM coupled with EDS was performed using Thermo Scientific Apreo 2 SEM equipped with the AZtec software platform (Oxford Instruments), at the University of Bristol. High-resolution electron images of the sample surface were captured under vacuum conditions at an accelerating voltage of 10 kV. Backscattered electron (BSE) detectors were utilized to observe surface morphology and compositional contrast.

Elemental analysis was conducted using Aztec software. Regions of interest were selected for point analysis using EDS. X-ray spectra were collected, and elements were identified based on their characteristic peaks. Semi-quantitative data were obtained from Aztec.

3. Results

In our incubation experiment, sediment and porewater samples were collected at one-year intervals and at the conclusion of the two-year period using distinct sampling strategies. Due to technical constraints, sediment samples taken at the one-year interval were limited to the upper few centimetres (Fig. 2), while at the two-year mark, sediments and porewaters from different depths were retrieved as a whole and homogenized. To evaluate whether different sample extraction strategies influenced the results, we also analysed two sets of incubated samples that had not been extracted at the year one interval. Similar ion and isotope compositions between these and the regularly extracted samples suggest that the extraction strategy had minimal impact on the geochemical signatures (Supplementary Fig. S4). Additionally, comparable elemental and isotopic compositions of porewater and overlying water across both time points suggest that the system had reached geochemical equilibrium by the end of the experiment (Supplementary Text S3, Fig. S5 and Fig. S6), further supporting the limited influence of sampling depth differences between the one-year and two-year intervals. Given the chemical homogeneity between the porewater and overlying water (Fig. S5 and Fig. S6), we infer that reactive conditions were uniform throughout the sediment column. This conclusion is further supported by the extensive authigenic precipitation observed on substrates located at the base of the tubes, which demonstrates that reactions were not depth restricted. However, we acknowledge that comparing partial sampling (Year one) with whole-core homogenization (Year two) relies on the assumption of vertical homogeneity.

3.1. Porewater samples

During the incubation period, the geochemical profile of the overlying waters closely resembled that of the porewater samples, indicating the well-mixed state between these two water bodies (Supplementary Text S3, Fig. S5 and Fig. S6). Hence, in the following discussion, we will mainly discuss the geochemical compositions in the porewater samples,

which can more closely reflect the geochemical dynamics during the incubation period. Additionally, the inserted substrates and biological activity impacted the geochemical dynamics within the porewater samples during the incubation, which is discussed in detail in the supplemental materials (Supplementary Text S4 and Text S5, Fig. S7 – S11). Overall, dissolution of the added substrates exerted the significant control on porewater chemistry. Extensive dissolution of glass beads releases large amounts of silicon, which lowers porewater δ^{30}Si. In contrast, kaolinite and quartz slow sediment dissolution through ion sorption. Because less light Si is released from the sediment, and as seawater-kaolinite interactions can lead to the rapid formation of authigenic phases (Zhang et al., 2021), which preferentially incorporate lighter Si isotopes (Geilert et al., 2024), porewaters in the kaolinite and quartz treatments retain higher δ^{30}Si values throughout the incubation (Supplementary Text S4 and Fig. 3). The presence of microbes in the non-sterile samples led to the microbially mediated anaerobic oxidation of Mn and Fe and formed Mn and Fe oxides (hereafter referred as BioMnFeOx). The BioMnFeOx can detain dissolved ions from porewater, this, combined with the scavenge of microbes, causing the substantial concentration gaps of a series of elements between the sterile and non-sterile samples (Supplementary Fig. S10). Furthermore, the consumption of lighter Si isotopes by microbes and removal of lighter Si isotopes by adsorption on BioMnFeOx has led to the heavier Si isotope composition in the non-sterile porewater sample (Supplementary Text S5 and Fig. S11). Microbial activity was most pronounced during the first year of incubation and declined in the second year, likely due to progressive nutrient limitation (Supplementary Text S5).

Compared to the one-year compositions, the concentrations of most elements remained stable or increased during the second year of incubation, while Fe and Al showed a drastic decline over the same period (Supplementary Fig. S10 – S12). The Si isotope compositions of the porewater samples exhibited substantial variability during two years of incubation, varying between −0.86 ‰ to +2.32 ‰ across all the porewater samples (Fig. 3).

3.2. Sediment samples

During the first year of incubation, Si content in both the Si-HCl and Si-Alk pools generally decreased, while their Si isotopic compositions increased. By the second year, Si content in both pools showed an overall increase (Fig. 4A and C). In the Si-HCl pool, Si isotope values became more variable across different samples compared to the first year, whereas in the Si-Alk pool, isotope values generally continued to increase (Fig. 4B and D). For comparison, the Si content and isotope ratios measured at year-zero and year-two in the Si-NaOH pool revealed an overall increase in Si content and a decrease in Si isotope composition over the two-year period (Fig. 4E and F).

3.3. SEM and EDS

After the termination of the incubation experiment, newly formed authigenic phases were observed on the surfaces of quartz sand and glass beads, in clear contrast to the originally smooth surfaces of the untreated quartz and glass beads (Fig. 5 and Fig. S13). The semi-quantitative analyses suggest that the newly formed authigenic phases mainly consist of Si, Al, Fe, K and Mg. The incorporation of Ca in the newly formed authigenic phases is only observed in the quartz substrates. (Fig. 5 and Fig. S13). It is important to note that our SEM analysis was conducted only on the substrates retrieved from the Teflon bags. This observation provided direct visual evidence for authigenic aluminosilicate formation on specific surfaces, and it is likely that authigenic phases also precipitated throughout the bulk incubated sediments (see section 4.1.2). These

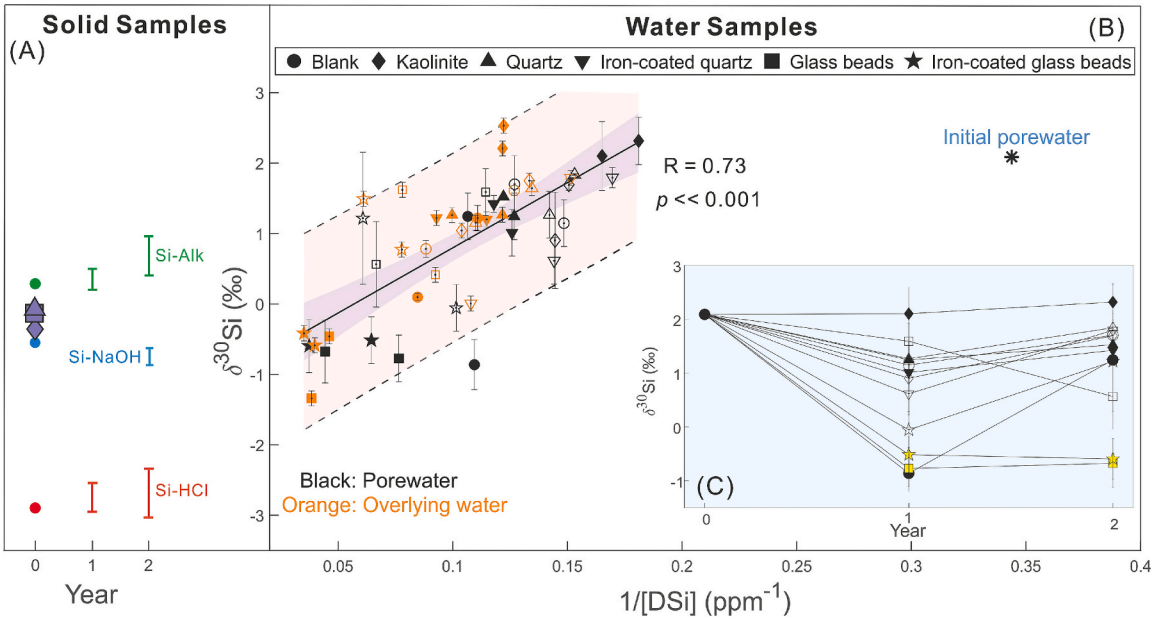

Fig. 3. Si isotopic composition of the incubated samples across the incubation period. In the solid sample box (A), three purple symbols show the Si isotope composition of three substrates. Red, blue and green dots and vertical bars represent the composition and range of Si isotopes of three Si pools extracted from sediments at year 0, year 1 and year 2, detailed isotopic evolution of these three Si pools is shown in Fig. 4. Water sample box (B) showing all the measured water samples throughout the course of incubation, solid symbols correspond to the sterilized sample set, while hollow symbols correspond to the non-sterilized sample set. The solid line represents the best-fit linear regression, with shaded areas indicating the 95% confidence interval and dashed lines showing the 95% prediction interval. The overall positive correlation between 1/DSi and δ^{30}Si suggests a broad control of substrate types on the Si isotope ratios (Supplementary Text S4.3). The black asterisk denotes the Si isotopic composition in the initial porewater sample, and the analytical uncertainty (1σ) of the initial porewater sample is smaller than the symbol size. The inset plot (C) shows the temporal evolution of porewater δ^{30}Si from year 0 to year 2 during incubation. Sterilized glass beads porewater samples are shown in yellow to highlight that the dissolution of glass beads overprinted the fractionation signals by reverse weathering type reactions. Error bars on the datapoints represent the procedural uncertainties between replicates of the same sample (1σ, n = 2 or 3). For samples that only had one replicate measured, the average procedural uncertainties were employed to present their uncertainties.

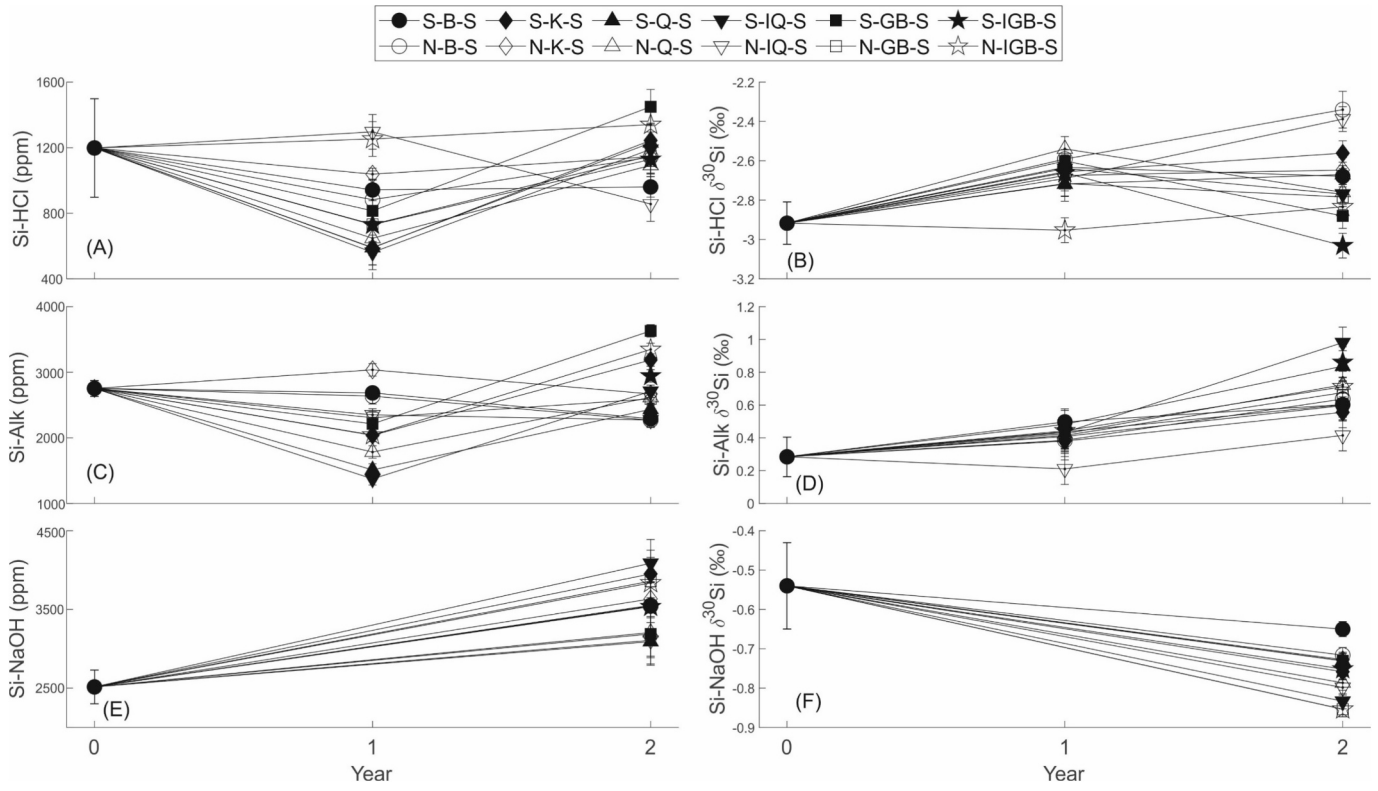

Fig. 4. Si content and Si isotopes of three Si pools: Si-HCl, Si-Alk and Si-NaOH in the sediment samples across two years of incubation. Error bars represent the analytical uncertainties for the initial samples (0 year, 1σ), and represent the procedural uncertainties between the replicates for the incubated samples (1σ). For samples that only had one replicate measured, the average procedural uncertainties were employed to present their uncertainties. Acronyms of samples are explained in Table 1.

sediment-hosted phases contribute to the Si isotopes measured in Si-HCl pools, but they were not examined microscopically and may differ mineralogically from the coatings observed on the substrates. SEM imaging was not performed for the kaolinite substrates and blank sediments due to the inherent difficulty in visually distinguishing authigenic precipitates from the underlying kaolinite/clay matrix. Nevertheless, chemical compositions in the porewater and sediment samples suggest that the formation of authigenic phases also likely occurred in kaolinites and blank sediments (see Section 4.1).

4. Discussion

Throughout the course of incubation, there were some observed changes that occurred across all samples, irrespective of the substrate types and sterilization conditions, suggesting the uniform control on the geochemistry in the incubation system. These uniform controls are discussed in the supplementary materials (Supplementary Text S6). In brief, these uniform controls include: (1) Ion diffusion from porewater to overlying water, (2) Possible reduction of Fe and Mn (hydro)oxides and (3) Partial dissolution of detrital secondary phases (Supplementary Text S6).

4.1. The occurrence of reverse weathering type reactions in the incubation experiment

4.1.1. Microscopic evidence of reverse weathering type reactions occurrence in the substrates

Authigenic cation-rich amorphous phases were found to be widely distributed across the surface of the quartz substrates (Fig. 5), indicating the occurrence of reverse weathering type reactions during the incubation period. Crucially, this authigenic phases formation occurred in both sterile and non-sterile samples (Fig. 5), revealing that the occurrence of reverse weathering type reactions does not require the presence of microbes under the tested conditions. As seen in the EDS spectra (Fig. 5), the abundance of different elements in these authigenic phases may vary slightly across different samples, but they primarily consist of Si, Al, Fe, K, Mg, Ca (Fig. 5). This elemental composition is in good agreement with those previously observed in authigenic phases formed through reverse weathering, characterized by a high cation content, particularly enriched in Al, Fe, and K (Loucaides et al., 2010; Mackin, 1987; Michalopoulos and Aller, 1995, 2004; Michalopoulos et al., 2000; Presti and Michalopoulos, 2008). The high abundance of Al and Fe in these newly formed authigenic phases explain the considerable decline of Al and Fe levels in porewaters in the second year of incubation (Supplementary Fig. S12 and Fig. S14). Although SEM and EDS analyses were not conducted on the kaolinite substrates, multiple lines of evidence suggest that authigenic phases also formed in the kaolinite incubations. Previous studies have shown that interactions between seawater and kaolinite can promote rapid neoformation of authigenic phases (Zhang et al., 2021). Consistent with this, during the second year of incubation, normalized Fe concentrations in kaolinite porewaters were lower than those in the glass bead treatments (Fig. S8), indicating more efficient removal of dissolved Fe. Given that authigenic phases formed in the glass bead samples (Supplementary Fig. S13), the enhanced Fe depletion in the kaolinite treatments implies similar or greater authigenic phase precipitation. This interpretation is further supported by persistently elevated δ^{30}Si values in kaolinite porewaters (Fig. 3B), consistent with ongoing authigenic phase formation.

Authigenic phases were rarely observed on glass beads, with elemental compositions similar to those in the quartz samples (Supplementary Fig. S13). This mirrors the findings of Michalopoulos and Aller (1995), where authigenic aluminosilicates predominantly formed between quartz grains but were scarcely seen on glass beads. This discrepancy may be due to i) the smooth surface of glass beads,

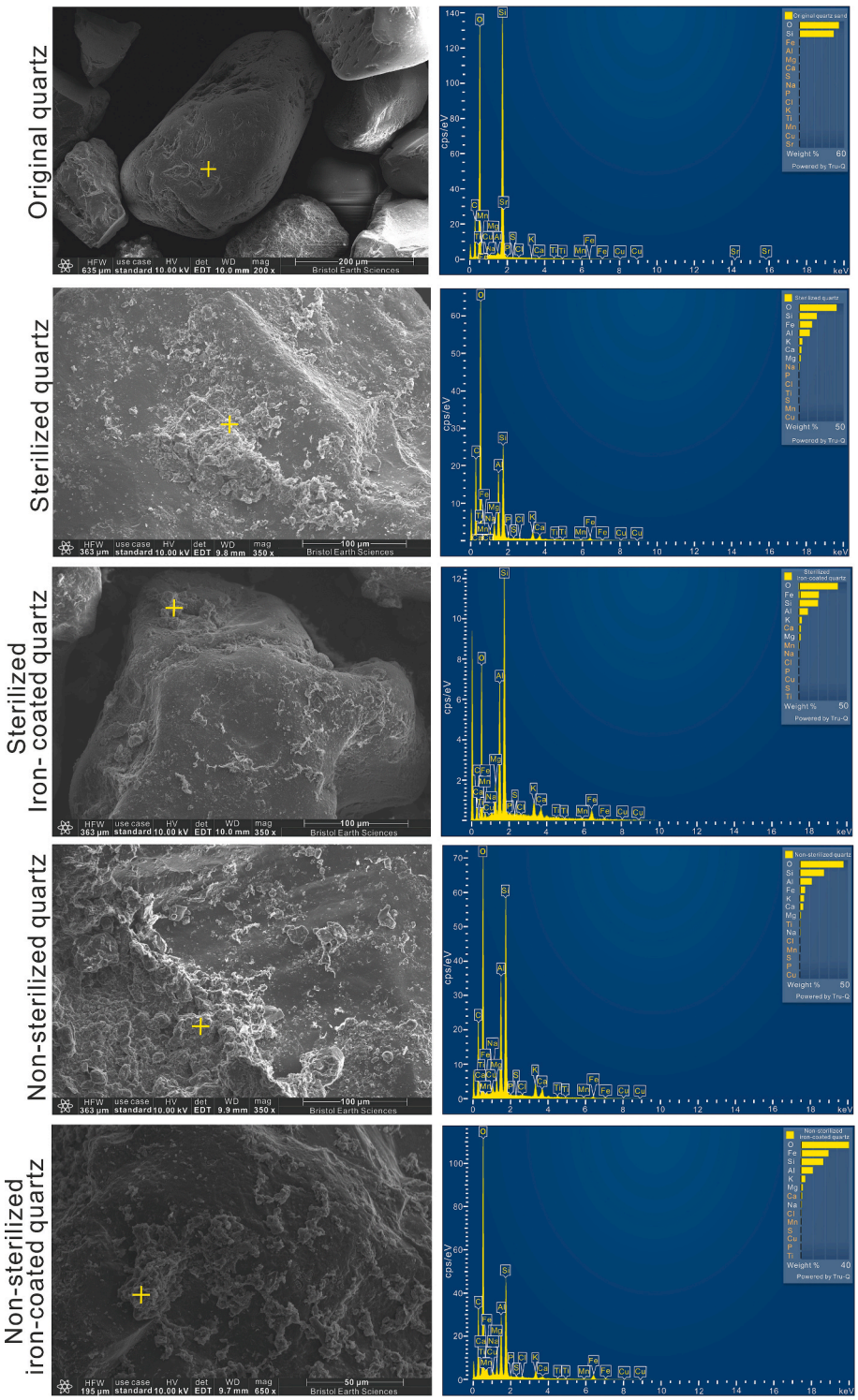

Fig. 5. SEM images and EDS spectra of the quartz substrates before and after two years of incubation, showing the prevalent occurrence of newly formed amorphous authigenic phases through reverse weathering type reactions during the incubation period. Yellow crosses indicate the area where EDS spectra were acquired. Authigenic phases were formed in both sterile and non-sterile samples, suggesting that the reverse weathering type reactions observed in this experiment do not require microbial involvement under the conditions tested.

which hinders the nucleation of the authigenic phases, and ii) the continuous dissolution of glass beads (Supplementary Text S4.6), which prevents stable attachment sites for the authigenic phases. It is important to note that, 1) in both Michalopoulos and Aller (1995) and the present study, these substrates primarily serve as visual indicators, and authigenic phases formation could also occur within the surrounding sediment matrix, 2) The glass beads used here to simulate BSi differ fundamentally from natural BSi. Natural diatom frustules possess high specific surface areas, intricate porous structures, and are typically associated with organic coatings rich in functional groups that can complex metal cations and lower the nucleation energy for authigenesis (Thakur et al., 2024). In contrast, the glass beads feature relatively smooth, non-porous surfaces. Our SEM observations, which show preferential authigenic phases formation on rougher quartz sand surfaces

rather than on the glass beads, corroborate this difference in surface reactivity.

4.1.2. Geochemical evidence of the occurrence of reverse weathering type reactions in the bulk sediment system

Based on the geochemical observations throughout the incubation duration, we have gained the following two findings about the occurrence of reverse weathering: i) the reverse weathering type reactions in the bulk sediment primarily occurred during the second year of incubation, and ii) the products of the reverse weathering type reactions, i.e., the newly formed authigenic phases, are closely associated with the Si-HCl pool in the sediments. It is important to note that the geochemical trends discussed in this section reflect the integrated response of the bulk sediment system and does not directly correspond to the specific authigenic phases observed on the introduced substrates (Fig. 5), which serve as localized indicators of authigenic precipitation.

4.1.2.1. The timing of reverse weathering type reactions in the bulk sediment during the incubation experiment. The finding that the reverse weathering type reactions primarily occurred during the second year of incubation is supported by several lines of geochemical evidence:

(1) Depletion of Fe and Al in porewaters in the second year:

Authigenic phases that form through reverse weathering type reactions are rich in Fe and Al (Ku and Walter, 2001; Li et al., 2021; Loucaides et al., 2010; Michalopoulos and Aller, 1995, 2004; Michalopoulos et al., 2000; Presti and Michalopoulos, 2008; Rahman et al., 2019; Van Bennekom et al., 1989; Zhang et al., 2022), such that the authigenesis reactions could be limited by Al and Fe availability (Ehlert et al., 2016; Presti and Michalopoulos, 2008; Zhao et al., 2025). In this study, the concentrations of dissolved Fe and Al in the porewater samples decreased dramatically during the second year of incubation, dropping from a few hundred ppb to over 1 ppm at year one, to <100 ppb or detectable levels (<20 ppb) at the end of incubation (Supplementary Fig. S12 and Fig. S14). It is important to note that the pronounced decline in Fe and Al concentrations is independent of their large procedural uncertainties (Supplementary Text S7, Fig. S14). This depletion of Fe and Al indicates uptake of these metals into a solid phase.

It should be noted alternative Fe sinks such as iron sulphides, Fe (hydro) oxides are unlikely to explain the observed geochemical trends, as they cannot account for the similarly strong and synchronous decrease in dissolved Al. The coupled decline of both Fe and Al therefore points to a common removal pathway, with authigenic phase formation being the most plausible explanation. Moreover, iron sulphide formation and biogenic Fe-oxide precipitation in marine sediments generally require microbial activity (e.g., Thiel et al., 2019), yet the most pronounced decreases in dissolved Fe and Al occurred in the sterile blank samples (Fig. S14), rather than in the non-sterilized treatments where biogenic Fe oxides were visually observed (Fig. S9). Together, these observations suggest that iron sulphide formation and biogenic Fe-oxide precipitation are likely insignificant under the conditions of our experiment.

By contrast, other key components in the newly formed authigenic phases, such as Si, K, Mg, and Ca, exhibit minimal depletion of their concentrations in the porewaters during the second year of incubation (Supplementary Fig. S12). This is likely due to their higher availability and continuous supply via sediment and substrate dissolution (Text S4 and Text S6), and, in the case of cations such as K^+, Mg^{2+} and Ca^{2+}, their reduced incorporation into authigenic phases during reverse weathering type reactions in comparison to Fe and Al (Zhao et al., 2025).

(2) Further enrichment of ^{30}Si in the porewater samples in the second year:

Si isotopic compositions in porewaters became heavier during the second year, even as biological activity declined (Supplementary Text S5). This isotopic shift is especially pronounced in the sterilized blank sample, indicating a non-biological driver resulting in the uptake of isotopically light Si, such as reverse weathering type reactions (Fig. 3C). In contrast, $\delta^{30}Si_{pw}$ values in the glass bead samples remained stable or decreased, reflecting ongoing dissolution of the glass beads. Previous studies have revealed that the dissolution of both biogenic and abiogenic silica preferentially releases the lighter Si isotopes (Demarest et al., 2009; Ziegler et al., 2005). Hence, the dissolution of the glass beads have overprinted any fractionation signal from authigenic precipitation (Fig. 3C).

(3) Emergence of a correlation between the Si isotopic compositions of the porewaters and the Si-HCl pool:

A positive correlation between $\delta^{30}Si_{pw}$ and Si isotope composition in the Si-HCl pools ($\delta^{30}Si_{HCl}$) appeared only after the second year (Fig. 6B), and was not observed after the first year (Fig. 6A), further suggesting that reverse weathering type reactions became a dominant process later in the incubation (See section 4.1.2.2.).

We also note that the sampling protocol at the Year 1 interval, which removed approximately 2 mL of overlying water (~25% of the aqueous phase) and a smaller proportion of the solid phase, effectively reduced the water/rock (W/R) ratio for the second year of the incubation. This reduction may have shifted conditions to be more favourable for authigenic precipitation, potentially contributing to the enhanced detectability of reverse weathering type reactions during the second year. However, the comparable geochemical compositions between samples subjected to Year 1 extraction and non-extracted controls (Fig. S4) suggest that the impact of the modified W/R ratio on overall system behaviour was limited.

In summary, during the first year of incubation, porewater and sediment geochemistry was primarily influenced by sediment and substrate dissolution, with biological activity additionally contributing in the non-sterilized samples. By the second year, as microbial influences diminished in the non-sterilized samples and the chemical environment stabilized in both treatments, reverse weathering type reactions became the dominant drivers of geochemical change. Additionally, the observed changes in DSi concentrations during the incubation experiment may provide some insight into the porewater DSi thresholds required for authigenic precipitation, although these constraints remain limited by the experimental design (Supplementary Text S8).

4.1.2.2. The role played by the sedimentary Si-HCl pool in the reverse weathering type reactions. Our data indicate that the newly formed authigenic phases are closely associated with the Si-HCl pool, supported by the following evidence:

(1) The erratic fractionation directions of $\delta^{30}Si_{HCl}$ in the second year of incubation:

During the second year of incubation, $\delta^{30}Si_{HCl}$ displayed inconsistent fractionation directions across samples, in contrast to the uniform shifts observed in Si-Alk pool ($\delta^{30}Si_{Alk}$) and Si-NaOH pool ($\delta^{30}Si_{NaOH}$) (Fig. 4B-F). Such variability in $\delta^{30}Si_{HCl}$ likely reflects the incorporation of newly formed authigenic phases into this pool, whose isotopic compositions vary depending on various factors, including local porewater conditions, reverse weathering intensity, diversity of secondary phases and the HCl leaching efficiency. Although sulphide formation (e.g., pyrite) could potentially influence $\delta^{30}Si_{HCl}$, as discussed in section 4.1.2.1, they are unlikely to significantly contribute the observed $\delta^{30}Si_{HCl}$ variation, given that the erratic fractionation patterns of $\delta^{30}Si_{HCl}$ are observed in both sterilized and non-sterilized samples (Fig. 6B).

(2) Significant correlation between $\delta^{30}Si_{HCl}$ and $\delta^{30}Si_{pw}$:

At the end of incubation, the Si isotopic values in the Si-HCl pool ($\delta^{30}Si_{HCl\_Y2}$) positively correlate with $\delta^{30}Si$ in porewaters ($\delta^{30}Si_{pw\_Y2}$), even in sterilized samples (Fig. 6B), implying that the Si-HCl pool has recorded the isotopic signature of the products from the reverse weathering type reactions.

This is consistent with the original purpose of HCl leaching introduced by Michalopoulos and Aller (2004), which aimed to remove metal oxides and poorly crystalline authigenic aluminosilicates, which, in this

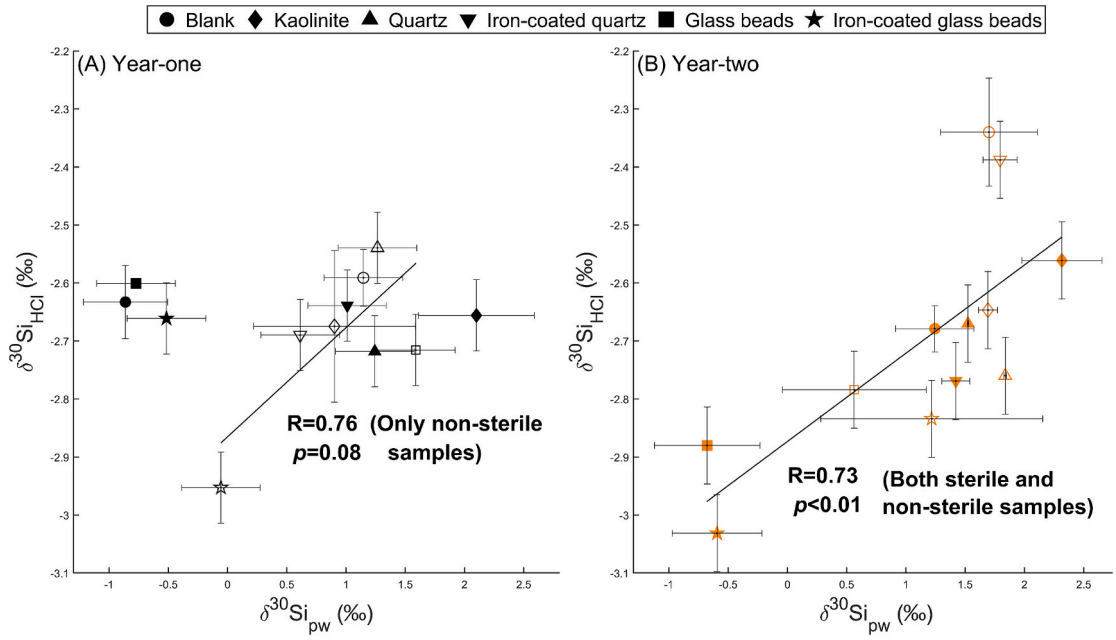

Fig. 6. Correlation of Si isotope ratios between the porewater samples and the Si-HCl pools in sediments: (A) Year-one samples and (B) Year-two samples. Solid symbols correspond to the sterilized samples, while hollow symbols correspond to the non-sterilized samples. Error bars represent the procedural uncertainties between different replicates of the same sample (1σ, n = 2 or 3). For samples that only had one replicate measured, the average procedural uncertainties were employed to present their uncertainties.

context, are likely the products of reverse weathering. Pickering et al. (2020) first identified extremely low δ^{30}Si values (−3.34 ‰ to −2.61 ‰) in Si-HCl pools, and similarly light Si isotope compositions have since been observed in the same operational pool extracted from sediments collected from other regions around the world (e.g., Huang et al., 2023; Ng et al., 2022; Wang et al., 2024; Ward et al., 2022). The authors proposed two possible pathways for the low δ^{30}Si values in the Si-HCl pool: (1) multistep processes involving BSi dissolution, authigenic precipitation, and oxide adsorption; or (2) the dissolution of isotopically lighter lithogenic silica (LSi). Due to the high abundance of LSi (20-fold larger than biogenic silica) and high dissolution rates in coastal environments.

Therefore, the rapid reprecipitation of this dissolved LSi could contribute to the extremely low δ^{30}Si values in the Si-HCl pool (Pickering et al., 2020).

Our incubation experiments enable us to interrogate this question from a different angle, through the isotopic changes in porewaters and Si-HCl pools over the course of incubation. The observed decrease of the $\delta^{30}Si_{NaOH}$ values during the incubation period indicates that the low $\delta^{30}Si_{HCl}$ values unlikely result from the dissolution and precipitation of LSi (Fig. 4F), which would instead leave the Si-NaOH pools with enriched ^{30}Si. Instead, the positive correlation between $\delta^{30}Si_{HCl\_Y2}$ and $\delta^{30}Si_{pw\_Y2}$ reveals the contribution from authigenic phases formation to the Si isotopic compositions in the Si-HCl pool.

Additional support comes from year-one data: the Si isotopic compositions in the Si-HCl pools ($\delta^{30}Si_{HCl\_Y1}$) in non-sterile samples showed greater variability than in sterile samples and a weak co-variation with the Si isotope composition in the porewater ($\delta^{30}Si_{pw\_Y1}$, Fig. 6A). Given the $\delta^{30}Si_{HCl\_Y1}$ compositions in the non-sterile samples were largely controlled by the DSi absorbed onto the Fe/Mn oxides (Supplementary Text S5.2), this suggests that Fe/Mn oxides also influenced isotopic signatures in the Si-HCl pool. Hence, our observations revealed that the $\delta^{30}Si_{HCl}$ compositions are affected by the authigenic phases formation and metal oxides adsorption, in accordance with the first pathway proposed by Pickering et al. (2020). This interpretation is also consistent with recent findings from Zhang et al. (2023), which demonstrated via leaching experiments that dilute HCl treatment effectively dissolves poorly crystalline authigenic secondary phases.

4.1.3. *Quantifying the silicon isotopic fractionation through reverse weathering*

The inherent difficulty in disentangling the mineralogical and geochemical signatures of reverse weathering from complex sediment matrices and overlapping biogeochemical processes limits direct determination of Si isotopic fractionation factors associated with reverse weathering type reactions. By incubating estuarine sediments under controlled and contrasting conditions, our experiment offers a unique opportunity to partially isolate reverse weathering type reactions and to constrain parameters across treatment, thereby providing insight into the Si isotope fractionation effects associated with these processes.

In this section, we aim to quantify the isotope fractionation effect of reverse weathering type reactions on the Si isotope composition ($^{30}\varepsilon_{RW\_authi\text{-}solution}$). The $^{30}\varepsilon_{RW\_authi\text{-}solution}$ can be assessed using the following equations (Eq. (1) and Eq. (2)).

$$^{30}\varepsilon_{RW_{authi-solution}} = \delta^{30}Si_{authi\_phases} - \delta^{30}Si_{pw\_post\_RW} \quad (1)$$

$$\delta^{30}Si_{pw\_post\_RW} = \delta^{30}Si_{pw\_Y1} + \Delta^{30}Si_{RW} \quad (2)$$

where $\delta^{30}Si_{authi\_phase}$ is the Si isotopic composition of the newly formed authigenic phases through reverse weathering, $\delta^{30}Si_{pw\_post\_RW}$ is the theoretical Si isotopic composition of porewater after reverse weathering. $\delta^{30}Si_{pw\_Y1}$ is the Si isotopic composition of the porewater sample at the one-year interval, and $\Delta^{30}Si_{RW}$ is the isotopic shift in porewater solely induced by reverse weathering. To isolate non-biological controls on Si isotopes, calculations in this section utilize only the sterilized sample. It should also be noted that calculation employed in this section is based on the two assumptions: (1) Authigenic phase formation was the dominant process controlling Si isotope variations during the second year of incubation. Other processes, such as Si uptake by Fe/Mn oxides, may also contribute. However, although Fe/Mn oxide formation was observed in the non-sterilized treatments (Supplementary Fig. S9), the largest δ^{30}Si shifts in both porewaters and Si–HCl pools are observed in the sterilized samples (S-B-PW, S-GB-S, and S-IGB-S; Fig. 3C and

Fig. 4B), suggesting that the contribution from Fe/Mn oxide is less significant than the precipitation of authigenic phases, (2) Reverse weathering type reactions in bulk sediment primarily occurred during the second year of incubation (Section 4.1.2.1).

The consistent $\delta^{30}Si_{pw}$ compositions, as well as the decreased $\delta^{30}Si_{HCl}$ compositions from year-one to year-two in the sterile glass bead samples (Fig. 4B) provide the opportunity to constrain the Si isotopic composition of the newly formed authigenic phases through reverse weathering type reactions ($\delta^{30}Si_{authi\_phases}$). These glass beads continuously dissolved, releasing DSi that controlled the $\delta^{30}Si_{pw}$ profile in the porewaters, resulting in the minimal shifts of $\delta^{30}Si_{pw}$ in the uncoated and iron-coated sterile glass bead porewater samples (S-GB-PW and S-IGB-PW, Fig. 3C) in the second year. Hence, these constant $\delta^{30}Si_{pw}$ values can be regarded as the Si isotopic composition in the 'initial solution', from which the authigenic phases formed. Also, the $\delta^{30}Si_{HCl}$ compositions in the uncoated and iron-coated glass bead sediment samples (S-GB-S and S-IGB-S) further decreased in the second year (Fig. 4B). The Si-HCl pool was already extremely enriched in ^{28}Si, in order to further decrease $\delta^{30}Si_{HCl}$, the newly formed authigenic phases must have lower Si isotope ratios than original $\delta^{30}Si_{HCl}$. The $\delta^{30}Si_{HCl\_Y2}$ compositions in the S-GB-S and S-IGB-S at the end of incubation were −2.88 ‰ ± 0.06 ‰ (1σ) and −3.03 ‰ ± 0.06 ‰ (1σ), respectively. This means that the newly formed authigenic phases in these two samples should at least equal or be even lower than −2.88 ‰ and −3.03 ‰ ($\delta^{30}Si_{authi\_phase} \leq -2.88$ ‰ and −3.03 ‰). If assuming that the $\delta^{30}Si_{pw\_Y2}$ values in the glass bead samples are the $\delta^{30}Si_{pw\_post\_RW}$ compositions (i.e., $\delta^{30}Si_{pw\_post\_RW}$ = −0.68 ‰ ± 0.45 ‰ (1σ) in S-GB-PW and −0.59 ‰ ± 0.38 ‰ (1σ) in S-IGB-PW), the $^{30}\varepsilon_{RW\_authi\text{-}solution}$ can be determined using the equation (Eq. (1)), which are −2.20 ‰ ± 0.45 ‰ (1σ) and −2.43 ‰ ± 0.38 ‰ (1σ).

However, we here argue that this is rather a conservative estimate, and the underestimation comes from two sources:

(1) The $\delta^{30}Si_{pw\_Y2}$ values in the glass bead samples were used as the $\delta^{30}Si_{pw\_post\_RW}$ compositions in equation (Eq. (1)). However, the real $\delta^{30}Si_{pw\_post\_RW}$ compositions should be higher than the $\delta^{30}Si_{pw\_Y2}$ values, as the fractionation imprint of Si isotope ratios by reverse weathering type reactions in the porewaters was masked by the extensive dissolution of glass beads during the second year of incubation (Fig. 3C).
(2) The actual $\delta^{30}Si_{authi\_phase}$ composition is likely to be lower than −2.88 ‰ or −3.03 ‰, given that this calculation only holds when it is the case that the newly formed authigenic phases are the dominant contributor of silica in the Si-HCl pool after two years of incubation. If the silica phase within the Si-HCl pool was still a mixture between the pre-existing silica and the newly formed authigenic phases, the $\delta^{30}Si_{authi\_phases}$ should be lighter than −2.88 ‰ and −3.03 ‰ ($\delta^{30}Si_{authi\_phase} >$ −2.88 ‰ or −3.03 ‰).

Therefore, the real $^{30}\varepsilon_{RW\_authi\text{-}solution}$ should be greater than −2.20 ‰ ± 0.45 ‰ (1σ) and −2.43 ‰ ± 0.38 ‰ (1σ), and −2.20 ‰ ± 0.45 ‰ (1σ) can be considered as the lower bound of the $^{30}\varepsilon_{RW\_authi\text{-}solution}$. To obtain an estimate that more closely reflects the real isotope fractionation effect, the isotopic shift in the porewater ($\Delta^{30}Si_{RW}$) can be further constrained. As established earlier, the geochemical composition in the porewater samples is substantially affected by the inserted substrates and the presence of microbes (Text S4 and Text S5). Hence, for simplicity, here we select the sterile blank sample (S-B) to constrain $\Delta^{30}Si_{RW}$ during the second year of incubation. The $\delta^{30}Si_{pw}$ of the S-B-PW sample increased from −0.86 ‰ ± 0.34 ‰ (1σ) to 1.24 ‰ ± 0.001 ‰ (1σ, reflecting the exceptionally high reproducibility of the substrate-free sterilized treatment) in the second year of incubation. This increase of $\delta^{30}Si_{pw}$ can be attributed to three processes: (1) Reverse weathering type reactions, (2) Dissolution of BSi, and (3) Isotope exchange between porewater and overlying water.

Our results indicate dynamic ion and isotope exchange between porewaters and overlying waters during incubation (Text S3), potentially leading to diffusion-driven isotopic fractionation. However, previous studies (Oelze et al., 2015; Richter et al., 2006) show such fractionation is minimal, and our S-B samples suggest equilibrium between porewaters and overlying waters. Therefore, diffusion-driven isotopic fractionation is not considered further.

Dissolution of BSi in marine sediments is a well-established major source of dissolved Si in porewaters and can promote the formation of authigenic phases (e.g., Michalopoulos and Aller, 1995; Zhao et al., 2025). Therefore, in the following calculation, BSi dissolution is assumed to be primary source of Si supplied to the porewaters. The occurrence of BSi dissolution in the second year is also supported by the depletion of ^{28}Si in the Si-Alk pools in sediments during the second year (Fig. 4D), which is indicative of the dissolution BSi and altered BSi. Therefore, when constraining $\Delta^{30}Si_{RW}$ in the S-P-BW sample, the isotopic shifts caused by BSi dissolution should also be factored in.

The effects of dissolution of BSi on the $\delta^{30}Si$ of DSi in the solution and the remaining BSi are poorly constrained. Demarest et al. (2009) reported an enrichment factor of −0.55 ‰ ($^{30}\varepsilon_{DSi\text{–}BSi} = -0.55$ ‰), while Wetzel et al. (2014) found little to no isotopic effect. In contrast, Sun et al. (2014) observed significant fractionation in DSi ($^{30}\varepsilon_{DSi\text{–}BSi}$ = −0.86 ‰) but no impact on residual BSi. Given the observed isotopic shifts in the Si-Alk pool during incubation (Fig. 4D), here we acknowledge the fractionation through BSi dissolution, and adopt −0.55 ‰ as the enrichment factor by BSi dissolution from Demarest et al. (2009) for the following calculation.

With this enrichment factor of −0.55 ‰ and the Si isotopic composition of the Si-Alk after the second year of incubation (denoted as $\delta^{30}Si_{Alk\_Y2}$, which is +0.6 ‰ ± 0.07 ‰, 1σ), the Si isotopic composition of the Si dissolved from the Si-Alk (denoted $\delta^{30}Si\text{-}Alk_{diss\_Y2}$) was calculated to be +0.05 ‰ ± 0.07 ‰ (1σ) ($\delta^{30}Si\text{-}Alk_{diss\_Y2}$ = +0.05 ‰ ± 0.07 ‰). Therefore, if no authigenic phases formation occurred during the second year of incubation, the $\delta^{30}Si_{pw}$ in the S-B-PW after two years should fall within the range between −0.86 ‰ ± 0.33 ‰ (1σ) and 0.05 ‰ ± 0.07 ‰ (1σ). The discrepancy between this expected $\delta^{30}Si_{pw}$ range and the measured $\delta^{30}Si_{pw}$ of +1.24 ‰ ± 0.001 ‰ (1σ) in the S-BP-W is +1.19 ‰ ± 0.07 ‰ (1σ) to +2.10 ‰ ± 0.33 ‰ (1σ), i.e., $\Delta^{30}Si_{RW}$ = +1.19 ± 0.07 ‰ (1σ) to +2.10 ‰ ± 0.33 ‰(1σ). It should be mentioned that this $\Delta^{30}Si_{RW}$ is also potentially an underestimation, as the dissolution of the Si-HCl pool was not considered in the calculation. The dissolution of the isotopically light Si-HCl pool could enrich the ^{28}Si in the porewater (Supplementary Text S6), thereby increasing the $\Delta^{30}Si_{RW}$.

With this newly obtained $\Delta^{30}Si_{RW}$, an updated $^{30}\varepsilon_{RW\_authi\text{-}solution}$ range can be calculated from the equations (Eq. (1) and Eq. (2)), which is −3.30 ‰ ± 0.34 ‰ (1σ) to −4.61 ‰ ± 0.47 ‰ (1σ). While calculating $\delta^{30}Si_{authi\_phases}$ and $\Delta^{30}Si_{RW}$ values from different treatments may introduce bias into the calculated $^{30}\varepsilon_{RW\_authi\text{-}solution}$ range, considering there were a few sources of underestimation when calculating the $\delta^{30}Si_{authi\_phases}$ and $\Delta^{30}Si_{RW}$ values, we believe this approach provides a reasonable and meaningful estimate, and the value of −4.61 ‰ ± 0.47 ‰ (1σ) is taken to be the upper bound of the $^{30}\varepsilon_{RW\_authi\text{-}solution}$. Therefore, the final $^{30}\varepsilon_{RW\_authi\text{-}solution}$ range estimated in this study is −2.20 ‰ ± 0.45 ‰ (1σ) to −4.61 ‰ ± 0.47 ‰ (1σ). Parameters and experiment conditions used for this calculation are summarized in the Supplementary Table S1.

This estimated $^{30}\varepsilon_{RW\_authi\text{-}solution}$ range is comparable or much higher than the $^{30}\varepsilon_{authi\text{-}solution}$ of −2.0 ‰ estimated by Ehlert et al. (2016) using a numerical model. However, we argue that to our knowledge, this study provides the first experimental estimation of silicon isotope fractionation during the formation of incipient authigenic phases, where the authigenic phases were freshly precipitated without going through the late diagenetic processes.

4.2. The impact of biology and substrate on the reverse weathering type reactions

In this section, we use the S-B sample, and our previous estimation of the isotopic fractionation effect via reverse weathering type reactions in this sample, to further investigate the impact of biology and substrates on early diagenesis. We assume that the isotopic shift of $\delta^{30}Si_{pw}$ during the second year of incubation (denoted $\Delta Si_{pw\_Y2\text{-}Y1}$, calculated via subtracting $\delta^{30}Si_{pw\_Y1}$ by $\delta^{30}Si_{pw\_Y2}$) can be used as indicator of the magnitude of fractionation by reverse weathering type reactions across different samples relative to the S-B "control". We caution that this approach is only comparative within the context of this two-year incubation, natural sedimentary systems exhibit far greater complexity, where sedimentation rates, open-system transport, and diverse mineral assemblages may induce fractionation pathways distinct from those observed in our closed-system sterile controls. Nevertheless, this internal comparison allows us to isolate the relative impact of microbial presence and substrate type on the early diagenetic signal under controlled conditions.

As shown in Fig. 7, the $\Delta Si_{pw\_Y2\text{-}Y1}$ values in the non-sterile samples are either higher or lower than those in the corresponding sterile samples. This variability likely reflects microbial activity, which can both preferentially uptake lighter Si isotopes, leading to higher $\Delta Si_{pw\_Y2\text{-}Y1}$ values, and consume key elements necessary for reverse weathering, thereby inhibiting the reaction and resulting in lower $\Delta Si_{pw\_Y2\text{-}Y1}$ values. For example, during the first year of incubation, the Fe and Al in the N-B-PW were removed by biological activity (Fe is a vital nutrient and both Al and Fe can be immobilized by the biological formed Fe and Mn oxides, Supplementary Text S5.1). After the first year of incubation, the dissolved Fe and Al level in the N-B-PW was approximately 4 to 6 times lower than that in the S-B-PW (Supplementary Fig. S12). Additionally, the generally higher procedural errors observed in the non-sterile samples compared to the sterile samples further suggest variable biological utilization of DSi across replicates (Supplementary Fig. S1 and S2).

The $\Delta Si_{pw\_Y2\text{-}Y1}$ values in the sterile kaolinite and quartz porewater samples are significantly lower than those observed in the sterile blank sample (Fig. 7). This likely reflects the distinct reaction kinetics induced by the added mineral substrates. In the sterile kaolinite and quartz treatments, porewater $\delta^{30}Si$ values were already elevated by the end of the first year, suggesting that the abundant mineral surfaces promoted rapid neoformation of authigenic phases. This interpretation is supported by the widespread occurrence of authigenic phases observed on quartz surfaces (Fig. 5) and the rapid formation of authigenic phases via the interaction between kaolinite and seawater observed by Zhang et al. (2021). Consistent with this, the sterilized kaolinite porewater sample at year one is the only treatment exhibiting higher $\delta^{30}Si$ values than the initial porewater (Fig. 3B), further supporting early authigenic phase formation. As a result, the values indicate that the sterile kaolinite and quartz systems approached equilibrium or saturation more rapidly than the mineral-poor S-B sample, effectively front-loading the isotopic fractionation signal into the first year.

The $\Delta Si_{pw\_Y2\text{-}Y1}$ values in the sterile glass bead samples are close to zero because the extensive dissolution of glass beads exerted the major control on the $\delta^{30}Si_{pw}$ and overprinted the fractionation signals from reverse weathering. This suggests that in an environment with abundant BSi, such as the western North Pacific Ocean (Shibamoto and Harada, 2010) or the Skagerrak strait (Spiegel et al., 2023), the extensive BSi dissolution could conceal the isotopic fractionation by reverse weathering.

4.3. Experimental constraints vs. natural estuarine dynamics

Given that the authigenic isotopic fractionation factors determined in this study were derived from a two-year closed incubation, it is critical to contextualize these quantitative constraints within the fundamental differences between our experimental boundary conditions and the dynamic natural environment. The incubation environment, characterized by the absence of advective flushing, solute renewal, or external oxidant supply, creates a biogeochemical trajectory that diverges from the sediment–water interface of the natural estuarine environment in three key ways.

(1) Redox oscillations and Fe-Mn cycling. In the natural estuaries, macrofaunal bioturbation and bio-irrigation introduce episodic pulses of oxygen deep into the sediment column. These oxidative incursions create micro-environments in which iron-oxidizing bacteria rapidly regenerate reactive Fe(III) (oxyhydr)oxides, thereby re-establishing oxidizing conditions and renewing redox reactivity within the sediment (Beam et al., 2018; Burdige, 2024). This continuous recycling of Fe oxides could potentially competes with reverse weathering reaction by sequestering dissolved Fe^{2+} and scavenging DSi via adsorption rather than authigenic incorporation. In contrast, our incubation experiment was carried out under anoxia, allowing the dissolved Fe^{2+} to accumulate without oxidative inhibition. This sustained reducing environment likely facilitate the formation of the authigenic phases.

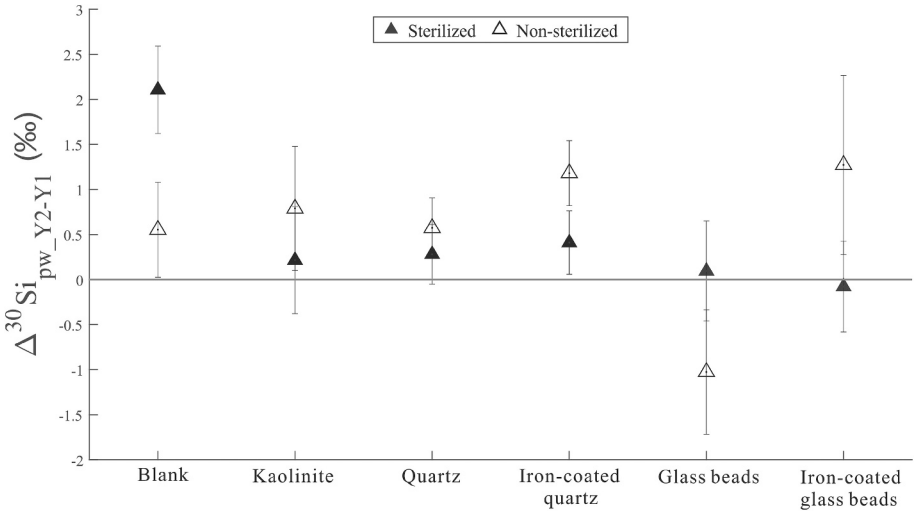

Fig. 7. The shift of Si isotopic compositions in the porewater samples during the second year of incubation ($\Delta Si_{pw\_Y2\text{-}Y1}$). Higher positive $\Delta Si_{pw\_Y2\text{-}Y1}$ values reflect higher magnitude of fractionation. Errors of the $\Delta Si_{pw\_Y2\text{-}Y1}$ values were propagated from the procedural errors from $\delta^{30}Si_{pw\_Y1}$ and $\delta^{30}Si_{pw\_Y2}$.

(2) Hydrodynamics and solute saturation. In natural estuaries, tidal pumping constantly moves water through the sediment, which keeps porewater chemical gradients from building up. In the field, this flushing often removes DSi before it can reach the high concentrations needed for new minerals to form (Wilson and Morris, 2012). In addition, frequent physical disturbances like resuspension can wear away any forming mineral coatings or expose fresh surfaces (Moriarty et al., 2021). This continual disruption prevents authigenic minerals from developing fully, unlike in our two-year laboratory experiment where conditions were undisturbed.
(3) Isotopic heterogeneity. While the closed system produced a strong isotopic shift in porewaters from the reverse weathering reactions because of the favourable conditions, the expression of this process in the field is likely far more heterogeneous. The natural estuarine floor consists of a patchwork of oxic and anoxic microenvironments (van Erk et al., 2023). Thus, the bulk porewater δ^{30}Si signature in the field often reflects an average of active authigenic zones and flushed, non-reactive zones.

Furthermore, variations in the water/rock (W/R) ratio may also play a role in modulating reverse weathering in natural systems. In our incubation, the reduced W/R ratio following Year 1 sampling may have contributed to conditions favourable for authigenic precipitation (Section 4.1.2.1). In natural settings, while the W/R ratio is generally much greater than in our experimental system, processes such as evaporation and tidal fluctuations can significantly reduce the W/R ratio in coastal lagoons and intertidal zones. These environments, where the W/R ratio is naturally reduced, may therefore be particularly conducive to reverse weathering and warrant further investigation in future field studies.

However, it is also important to recognize that dynamic nature of the open estuary also possesses specific mechanisms that may enhance reverse weathering relative to our static incubations. First, the oscillating redox cycles driven by bioturbation continuously generate fresh, high surface area Fe-(oxyhydr)oxides. The subsequent reductive dissolution of these reactive phases provides a recurring pulse of highly reactive Fe^{2+} that is kinetically superior to the aged iron pools in a static system (Beam et al., 2022). Second, as proposed by Aller, 1998, constant physical stirring and mixing at the estuary bottom keeps sediments in a dynamic, ‘‘fluidized’’ state (Chen et al., 2022). This continual abrasion of grain surfaces prevents them from developing protective coatings or becoming chemically inactive, a process that likely slowed reactions in our static lab incubations. Finally, and most importantly, the continuous supply of riverine suspended particulate matters and groundwater solutes can provide the key reactants for the reverse weathering reactions, including the reactive aluminosilicates, DSi, BSi and iron (Guo et al., 2024; Loucaides et al., 2010; Oh et al., 2023; Zhang et al., 2024), whereas our closed system was strictly limited by the finite reservoir of detritus.

In conclusion, both open and closed systems are characterised by biogeochemical processes that could promote reverse weathering type reactions: while the closed incubation removes transport limitations to maximize thermodynamic saturation, the open field systems leverages physical and redox dynamics to maximize substrate reactivity. Significant silicon isotope fractionation associated with reverse weathering type reactions has been observed in natural open systems (Geilert et al., 2024; Geilert et al., 2020). Moreover, the origin of the extremely low δ^{30}Si values measured in the Si–HCl pool of sediments worldwide remains poorly constrained (Ng et al., 2022; Pickering et al., 2020; Wang et al., 2024; Ward et al., 2022). The fractionation factors determined in this study therefore provide valuable mechanistic insight into reverse weathering type reactions and offer a framework that can be extended to natural open systems to help reconcile large silicon isotope fractionations. However, such applications should be approached with caution, given the inherent differences between experimentally constrained closed systems and natural open systems.

5. Conclusions

This study demonstrates that reverse weathering type reactions could play a significant role in shaping the geochemistry in marine sediments. The two-year sediment incubation experiment revealed substantial silicon isotope fractionation in porewaters and Si-HCl pools, with shifts in δ^{30}Si ranging from +2.2 ‰ ± 0.45 ‰ (1σ) to +4.61 ‰ ± 0.47 ‰ (1σ) ($^{30}\varepsilon_{RW_authi\text{-}solution}$ = −2.2 ‰ ± 0.45 ‰ to −4.61 ‰ ± 0.47 ‰). This high fractionation may help explain the strongly fractionated Si isotope compositions observed in both reactive solid-phase pools and pore fluids where reverse weathering type reactions is active. These findings suggest that reverse weathering can exert a much stronger influence on silicon isotope signatures than previously recognized, with implications for the global Si isotope budget across diverse environments. While reverse weathering type reactions can occur in the absence of microbes, the presence of microbial activity and inserted substrates, representing varying sediment compositions, were found to significantly influence the extent of the reaction. These results underscore the complex interactions between biological activity, sediment composition, and reverse weathering, highlighting the need for a more nuanced understanding of how these processes operate in different environments.

Data availability

Data are available through Zenodo at https://doi.org/10.5281/zenodo.15738951.

CRediT authorship contribution statement

Zhe Dong: Writing – review & editing, Writing – original draft, Visualization, Methodology, Investigation, Formal analysis, Data curation, Conceptualization. **Katharine Hendry:** Writing – review & editing, Supervision, Methodology, Funding acquisition. **James M. Byrne:** Writing – review & editing, Supervision, Methodology. **Casey Bryce:** Writing – review & editing, Supervision, Methodology. **Tong Wang:** Writing – review & editing, Methodology. **Hong Chin Ng:** Writing – review & editing, Methodology. **Jamie Lewis:** Writing – review & editing, Methodology.

Declaration of competing interest

The authors declare that they have no known competing financial interests or personal relationships that could have appeared to influence the work reported in this paper.

Acknowledgements

We thank Christopher Coath, Harry Forrester, Katie O'Neill and Carolyn Taylor for their help with laboratory work. Z. Dong was funded by a CSC-UoB Joint Scholarship. K. Hendry is funded by Natural Environment Research Council grant SiCLING (Silicon Cycling in Glaciated Environments) (grant no. NE/X014819/1).

Appendix A. Supplementary material

The supplementary material includes texts and figures that support the main findings illustrated in the main text, including data reproducibility, radiogenic Sr isotope composition, influences of inserted substrates and biological activity on the geochemistry in the incubation system, uniform controls in the incubation system and replicate-level of comparison of Al and Fe concentrations in porewaters in the second year. Supplementary material to this article can be found online at https://doi.org/10.1016/j.gca.2026.04.015.

References

Allen, J.R.L., 1991. Fine sediment and its sources, Severn Estuary and inner Bristol Channel, southwest Britain. Sed. Geol. 75 (1), 57–65.

Aller, R.C., 1998. Mobile deltaic and continental shelf muds as suboxic, fluidized bed reactors. Mar. Chem. 61 (3), 143–155.

Beam, J.P., Michaud, A.B., Johnston, D.T., Girguis, P.R., Emerson, D., 2022. Impacts of bioturbation on iron biogeochemistry and microbial communities in coastal sediment mesocosms under varying degrees of hypoxia. Estuar. Coast. Shelf Sci. 276, 108032.

Beam, J.P., Scott, J.J., McAllister, S.M., Chan, C.S., McManus, J., Meysman, F.J.R., Emerson, D., 2018. Biological rejuvenation of iron oxides in bioturbated marine sediments. ISME J. 12 (5), 1389–1394.

Burdige, D.J., 2024. 3.18 - Estuarine and coastal sediments – coupled biogeochemical cycling. In: Baird, D., Elliott, M. (Eds.), Treatise on Estuarine and Coastal Science, Second Edition. Academic Press, Oxford, pp. 578–625.

Cardinal, D., Alleman, L.Y., de Jong, J., Ziegler, K., André, L., 2003. Isotopic composition of silicon measured by multicollector plasma source mass spectrometry in dry plasma mode. J. Anal. At. Spectrom. 18 (3), 213–218.

Chen, Y.-J., Leung, P.M., Cook, P.L.M., Wong, W.W., Hutchinson, T., Eate, V., Kessler, A. J., Greening, C., 2022. Hydrodynamic disturbance controls microbial community assembly and biogeochemical processes in coastal sediments. ISME J. 16 (3), 750–763.

De la Rocha, C.L., 2002. Measurement of silicon stable isotope natural abundances via multicollector inductively coupled plasma mass spectrometry (MC-ICP-MS). Geochem. Geophys. Geosyst. 3.

de Souza, G.F., Reynolds, B.C., Rickli, J., Frank, M., Saito, M.A., Gerringa, L.J.A., Bourdon, B., 2012. Southern Ocean control of silicon stable isotope distribution in the deep Atlantic Ocean. Global Biogeochem. Cycles 26.

Demarest, M.S., Brzezinski, M.A., Beucher, C.P., 2009. Fractionation of silicon isotopes during biogenic silica dissolution. Geochim. Cosmochim. Acta 73 (19), 5572–5583.

Demaster, D.J., 1981. The supply and accumulation of silica in the marine-environment. Geochim. Cosmochim. Acta 45 (10), 1715–1732.

Ehlert, C., Doering, K., Wallmann, K., Scholz, F., Sommer, S., Grasse, P., Geilert, S., Frank, M., 2016. Stable silicon isotope signatures of marine pore waters - biogenic opal dissolution versus authigenic clay mineral formation. Geochim. Cosmochim. Acta 191, 102–117.

Gebco Bathymetric Compilation Group. (2022). The GEBCO_2022 Grid - a continuous terrain model of the global oceans and land.

Geilert, S., Frick, D.A., Abbott, A.N., Löhr, S.C., 2024. Marine clay maturation induces systematic silicon isotope decrease in authigenic clays and pore fluids. Commun. Earth Environ. 5 (1), 573.

Geilert, S., Grasse, P., Doering, K., Wallmann, K., Ehlert, C., Scholz, F., Frank, M., Schmidt, M., Hensen, C., 2020. Impact of ambient conditions on the Si isotope fractionation in marine pore fluids during early diagenesis. Biogeosciences 17 (6), 1745–1763.

Geilert, S., Vroon, P.Z., Roerdink, D.L., Van Cappellen, P., van Bergen, M.J., 2014. Silicon isotope fractionation during abiotic silica precipitation at low temperatures: inferences from flow-through experiments. Geochim. Cosmochim. Acta 142, 95–114.

Grasse, P., Brzezinski, M.A., Cardinal, D., de Souza, G.F., Andersson, P., Closset, I., Cao, Z.M., Dai, M.H., Ehlert, C., Estrade, N., Francois, R., Frank, M., Jiang, G.B., Jones, J.L., Kooijman, E., Liu, Q., Lu, D.W., Pahnke, K., Ponzevera, E., Schmitt, M., Sun, X., Sutton, J.N., Thil, F., Weis, D., Wetzel, F., Zhang, A., Zhang, J., Zhang, Z.L., 2017. GEOTRACES inter-calibration of the stable silicon isotope composition of dissolved silicic acid in seawater. J. Anal. At. Spectrom 32 (3), 562–578.

Guo, Z., Chen, M., Ouyang, W., Lin, C., He, M., 2024. Fine particle contents in sediment drive silica transport and deposition to the estuary in the turbid river basin. Water Res. 255, 121464.

Hendry, K.R., Leng, M.J., Robinson, L.F., Sloane, H.J., Blusztjan, J., Rickaby, R.E.M., Georg, R.B., Halliday, A.N., 2011. Silicon isotopes in Antarctic sponges: an interlaboratory comparison. Antarct. Sci. 23 (1), 34–42.

Huang, T.-H., Sun, X., Somelar, P., Kirsimäe, K., Pickering, R.A., Kim, J.-H., Kielman-Schmitt, M., Hong, W.-L., 2023. Separating Si phases from diagenetically-modified sediments through sequential leaching. Chem. Geol. 637, 121681.

Huang, T.Z., Shen, B., Wang, X.L., Ma, H.R., Li, C., Zhou, C.M., 2024. Extremely ^{26}Mg-enriched authigenic clays from the Ediacaran Doushantuo Formation (South China) indicating the coupled carbonate-silicate diagenesis. Global Planet. Change 239.

Hughes, H.J., Sondag, F., Cocquyt, C., Laraque, A., Pandi, A., André, L., Cardinal, D., 2011. Effect of seasonal biogenic silica variations on dissolved silicon fluxes and isotopic signatures in the Congo River. Limnol. Oceanogr. 56 (2), 551–561.

Isson, T.T., Planavsky, N.J., 2018. Reverse weathering as a long-term stabilizer of marine pH and planetary climate. Nature 560 (7719), 471-+.

Karl, D.M., Tien, G., 1992. Magic - a sensitive and precise method for measuring dissolved phosphorus in aquatic environments. Limnol. Oceanogr. 37 (1), 105–116.

Kirby, R., 2010. Distribution, transport and exchanges of fine sediment, with tidal power implications: Severn Estuary, UK. Mar. Pollut. Bull. 61 (1–3), 21–36.

Ku, T.C.W., Walter, L.M., 2001. Rapid authigenic ferric clay formation in shallow marine tropical sendiments: environmental controls and implications for major elemental cycles. Paper presented at the Goldschmidt Conference (2001).

Langston, W.J., Jonas, P.J.C., Millward, G.E., 2010. The severn estuary and bristol channel: a 25 year critical review. Mar. Pollut. Bull. 61 (1–3), 1–4.

Li, F.B., Penman, D., Planavsky, N., Knudsen, A., Zhao, M.Y., Wang, X.L., Isson, T., Huang, K.J., Wei, G.Y., Zhang, S., Shen, J., Zhu, X.K., Shen, B., 2021. Reverse weathering may amplify post-Snowball atmospheric carbon dioxide levels. Precambr. Res. 364.

Lin, C.Y., Abdullah, M.H., Musta, B., Praveena, S.M., Aris, A.Z., 2011. Stability behavior and thermodynamic states of iron and manganese in sandy soil aquifer, Manukan Island, Malaysia. Natl. Resour. Res. 20 (1), 45–56.

Loucaides, S., Michalopoulos, P., Presti, M., Koning, E., Behrends, T., Van Cappellen, P., 2010. Seawater-mediated interactions between diatomaceous silica and terrigenous sediments: results from long-term incubation experiments. Chem. Geol. 270 (1–4), 68–79.

Mackenzie, F.T., Garrels, R.M., 1966. Chemical mass balance between rivers and oceans. Am. J. Sci. 264 (7), 507-+.

Mackenzie, F.T., Kump, L.R., 1995. Reverse weathering, clay mineral formation, and oceanic element cycles. Science 270 (5236), 586–587.

Mackin, J.E., 1987. Boron and silica behavior in salt-marsh sediments - implications for paleo-boron distributions and the early diagenesis of silica. Am. J. Sci. 287 (3), 197–241.

Manning, A.J., Langston, W.J., Jonas, P.J.C., 2010. A review of sediment dynamics in the severn estuary: influence of flocculation. Mar. Pollut. Bull. 61 (1–3), 37–51.

März, C., Meinhardt, A.K., Schnetger, B., Brumsack, H.J., 2015. Silica diagenesis and benthic fluxes in the Arctic Ocean. Mar. Chem. 171, 1–9.

Massmann, G., Pekdeger, A., Merz, C., 2004. Redox processes in the Oderbruch polder groundwater flow system in Germany. Appl. Geochem. 19 (6), 863–886.

Michalopoulos, P., Aller, R.C., 1995. Rapid clay mineral formation in amazon delta sediments - reverse weathering and oceanic elemental cycles. Science 270 (5236), 614–617.

Michalopoulos, P., Aller, R.C., 2004. Early diagenesis of biogenic silica in the Amazon delta: alteration, authigenic clay formation, and storage. Geochim. Cosmochim. Acta 68 (5), 1061–1085.

Michalopoulos, P., Aller, R.C., Reeder, R.J., 2000. Conversion of diatoms to clays during early diagenesis in tropical, continental shelf muds. Geology 28 (12), 1095–1098.

Moriarty, J.M., Friedrichs, M.A.M., Harris, C.K., 2021. Seabed resuspension in the chesapeake bay: implications for biogeochemical cycling and hypoxia. Estuar. Coasts 44 (1), 103–122.

Mortlock, R.A., Froelich, P.N., 1989. A simple method for the rapid-determination of biogenic opal in pelagic marine-sediments. Deep-Sea Res. Part A-Oceanographic Res. Papers 36 (9), 1415–1426.

Ng, H.C., Cassarino, L., Pickering, R.A., Woodward, E.M.S., Hammond, S.J., Hendry, K. R., 2020. Sediment efflux of silicon on the Greenland margin and implications for the marine silicon cycle. Earth Planet. Sci. Lett. 529.

Ng, H.C., Hawkings, J.R., Bertrand, S., Summers, B.A., Sieber, M., Conway, T.M., Freitas, F.S., Ward, J.P.J., Pryer, H.V., Wadham, J.L., Arndt, S., Hendry, K.R., 2022. Benthic dissolved silicon and iron cycling at glaciated patagonian fjord heads. Global Biogeochem. Cycles 36 (11) e2022GB007493.

Oelze, M., von Blanckenburg, F., Bouchez, J., Hoellen, D., Dietzel, M., 2015. The effect of Al on Si isotope fractionation investigated by silica precipitation experiments. Chem. Geol. 397, 94–105.

Oh, Y.H., Kim, J., Kim, G., Kim, T.H., 2023. Groundwater as a source of phosphorus and silicate in an estuarine zone: results from continuous monitoring of nutrients and ^{222}Rn. Front. Mar. Sci. 10.

Pickering, R.A., Cassarino, L., Hendry, K.R., Wang, X.L.L., Maiti, K., Krause, J.W., 2020. Using stable isotopes to disentangle marine sedimentary signals in reactive silicon pools. Geophys. Res. Lett. 47 (15).

Presti, M., Michalopoulos, P., 2008. Estimating the contribution of the authigenic mineral component to the long-term reactive silica accumulation on the western shelf of the Mississippi River Delta. Cont. Shelf Res. 28 (6), 823–838.

Rahman, S., Aller, R.C., Cochran, J.K., 2016. Cosmogenic ^{32}Si as a tracer of biogenic silica burial and diagenesis: major deltaic sinks in the silica cycle. Geophys. Res. Lett. 43 (13), 7124–7132.

Rahman, S., Aller, R.C., Cochran, J.K., 2017. The missing silica sink: revisiting the marine sedimentary Si cycle using cosmogenic ^{32}Si. Global Biogeochem. Cycles 31 (10), 1559–1578.

Rahman, S., Tamborski, J.J., Charette, M.A., Cochran, J.K., 2019. Dissolved silica in the subterranean estuary and the impact of submarine groundwater discharge on the global marine silica budget. Mar. Chem. 208, 29–42.

Reynolds, B.C., Aggarwal, J., André, L., Baxter, D., Beucher, C., Brzezinski, M.A., Engström, E., Georg, R.B., Land, M., Leng, M.J., Opfergelt, S., Rodushkin, I., Sloane, H.J., van den Boorn, S.H.J.M., Vroon, P.Z., Cardinal, D., 2007. An inter-laboratory comparison of Si isotope reference materials. J. Anal. At. Spectrom 22 (5), 561–568.

Richter, F.M., Mendybaev, R.A., Christensen, J.N., Hutcheon, I.D., Williams, R.W., Sturchio, N.C., Beloso, A.D., 2006. Kinetic isotopic fractionation during diffusion of ionic species in water. Geochim. Cosmochim. Acta 70 (2), 277–289.

Santiago Ramos, D.P., Morgan, L.E., Lloyd, N.S., Higgins, J.A., 2018. Reverse weathering in marine sediments and the geochemical cycle of potassium in seawater: insights from the K isotopic composition (^{41}K/^{39}K) of deep-sea pore-fluids. Geochim. Cosmochim. Acta 236, 99–120.

Severn Estuary Partnership. (2025). Severn Estuary Partnership, https://severnestuarypartnership.org.uk/the-estuary/environmental-quality/weather-and-climate-change/ [Accessed 21 March 2025].

Shibamoto, Y., Harada, K., 2010. Silicon flux and distribution of biogenic silica in deep-sea sediments in the western North Pacific Ocean. Deep Sea Res. Part I 57 (2), 163–174.

Sorwat, J., Mellage, A., Kappler, A., Byrne, J.M., 2020. Immobilizing magnetite onto quartz sand for chromium remediation. J. Hazard. Mater. 400.

Spiegel, T., Dale, A.W., Lenz, N., Schmidt, M., Sommer, S., Kalapurakkal, H.T., Przibilla, A., Lindhorst, S., Wallmann, K., 2023. Biogenic silica cycling in the Skagerrak. Front. Mar. Sci. 10–2023.

Stookey, L.L., 1970. Ferrozine - a new spectrophotometric reagent for iron. Anal. Chem. 42 (7), 779.
Sun, X., Olofsson, M., Andersson, P.S., Fry, B., Legrand, C., Humborg, C., Mörth, C.M., 2014. Effects of growth and dissolution on the fractionation of silicon isotopes by estuarine diatoms. Geochim. Cosmochim. Acta 130, 156–166.
Thakur, B., Shrivastava, R., Gupta, V.K., Nadda, A.K., 2024. Biogenic silica: sources, structure and properties. In: Nadda, A.K., Gupta, V.K. (Eds.), Biogenic Silica: Fundamentals and Applications. Royal Society of Chemistry.
Thiel, J., Byrne, J.M., Kappler, A., Schink, B., Pester, M., 2019. Pyrite formation from FeS and H(2)S is mediated through microbial redox activity. PNAS 116 (14), 6897–6902.
Trapp-Müller, G., Caves Rugenstein, J., Conley, D.J., Geilert, S., Hagens, M., Hong, W.-L., Jeandel, C., Longman, J., Mason, P.R.D., Middelburg, J.J., Milliken, K.L., Navarre-Sitchler, A., Planavsky, N.J., Reichart, G.-J., Slomp, C.P., Sluijs, A., van Hinsbergen, D.J.J., Zhang, X.Y., 2025. Earth's silicate weathering continuum. Nat. Geosci. 18 (8), 691–701.
Van Bennekom, A.J., Jansen, J.H.F., Vandergaast, S.J., Vaniperen, J.M., Pieters, J., 1989. Aluminum-rich opal - an intermediate in the preservation of biogenic silica in the Zaire (Congo) deep-sea fan. Deep-Sea Res. Part A-Oceanographic Res. Papers 36 (2), 173–190.
van Erk, M.R., Bourceau, O.M., Moncada, C., Basu, S., Hansel, C.M., de Beer, D., 2023. Reactive oxygen species affect the potential for mineralization processes in permeable intertidal flats. Nat. Commun. 14 (1), 938.
Wallington, H., Hendry, K., Perkins, R., Yallop, M., Arndt, S., 2023. Benthic diatoms modify riverine silicon export to a marine zone in a hypertidal estuarine environment. Biogeochemistry 162 (2), 177–200.
Wang, K., Li, W., Li, S., Tian, Z., Koefoed, P., Zheng, X.-Y., 2021. Geochemistry and cosmochemistry of potassium stable isotopes. Geochemistry 81 (3), 125786.
Wang, T., Ng, H.C., Hatton, J.E., Hammond, S.J., Woodward, E.M.S., Meire, L., Hendry, K.R., 2024. Silicon isotopes reveal the impact of fjordic processes on the transport of reactive silicon from glaciers to coastal regions. Chem. Geol. 670.
Ward, J.P.J., Hendry, K.R., Arndt, S., Faust, J.C., Freitas, F.S., Henley, S.F., Krause, J.W., Marz, C., Ng, H.C., Pickering, R.A., Tessin, A.C., 2022. Stable silicon isotopes uncover a mineralogical control on the benthic silicon cycle in the Arctic Barents Sea. Geochim. Cosmochim. Acta 329, 206–230.
Wetzel, F., de Souza, G.F., Reynolds, B.C., 2014. What controls silicon isotope fractionation during dissolution of diatom opal? Geochim. Cosmochim. Acta 131, 128–137.
Wilson, A.M., Morris, J.T., 2012. The influence of tidal forcing on groundwater flow and nutrient exchange in a salt marsh-dominated estuary. Biogeochemistry 108 (1), 27–38.
Zhang, X., Bajard, M., Bouchez, J., Sabatier, P., Poulenard, J., Arnaud, F., Crouzet, C., Kuessner, M., Dellinger, M., Gaillardet, J., 2023. Evolution of the alpine critical zone since the last glacial period using Li isotopes from lake sediments. Earth Planet. Sci. Lett. 624, 118463.
Zhang, X., Gaillardet, J., Barrier, L., Bouchez, J., 2022. Li and Si isotopes reveal authigenic clay formation in a palaeo-delta. Earth Planet. Sci. Lett. 578.
Zhang, X., Saldi, G.D., Schott, J., Bouchez, J., Kuessner, M., Montouillout, V., Henehan, M., Gaillardet, J., 2021. Experimental constraints on Li isotope fractionation during the interaction between kaolinite and seawater. Geochim. Cosmochim. Acta 292, 333–347.
Zhang, Z., Zhang, G., Zhao, Y., Liu, C., Liu, S., Yang, J., Guo, X., Wei, H., Li, S., 2024. Transportation and transformation of sedimentary Fe speciation in the northern South China Sea. J. Asian Earth Sci. 276, 106371.
Zhao, S., Saad, E.M., Pickering, R.A., Liu, P., Zuo, H., Zhao, L., Ingall, E., Taillefert, M., Reinhard, C.T., Dong, H., Krause, J.W., Tang, Y., 2025. Rapid transformation of biogenic silica to authigenic clay: mechanisms and geochemical constraints. Sci. Adv. 11 (44), eadt3374.
Ziegler, K., Chadwick, O.A., Brzezinski, M.A., Kelly, E.F., 2005. Natural variations of δ^{30}Si ratios during progressive basalt weathering, Hawaiian Islands. Geochim. Cosmochim. Acta 69 (19), 4597–4610.